Check for updates

Performance evaluation of Eu$_2$NiMnO$_6$-based lead-free perovskite solar cells: a SCAPS-1D study

Md. Abu Bakkar Siddique,[ab] Nazmul Shahadath,[ab] Md. Tarekuzzaman, [ab]
Md. Raihan Kabir,[ab] Sohail Ahmad,[c] Rashel Mohammad Khokan,*[abd]
Md. Rasheduzzaman,[ab] S. M. G. Mostafa,[b] Mohammad Jalal Uddin[b]
and Md. Zahid Hasan [*ab]

Lead-free double Perovskite materials are currently attracting considerable research interest owing to their environmentally friendly attributes. In this investigation, we have analyzed a tremendous double Perovskite material Eu$_2$NiMnO$_6$ (ENMO) as the absorber layer of a solar cell with the help of SCAPS-1D (a solar cell capacitance simulator). The material has become remarkable because of its narrow experimental band gap of 1.01 eV. Throughout the study, we investigated the effect of appropriate ETLs (Electron Transport Layers) and HTLs (Hole Transport Layers) with the absorber layer. For optimizing the device, tungsten disulfide (WS$_2$), C$_{60}$ (Buckminsterfullerene), and PCBM (Phenyl-C$_{61}$-butyric acid methyl ester) are used as ETLs, and Copper Ferrite Tin Sulfide (CFTS) is used as the HTL. Besides evaluating the effects of ETL and HTL, other important factors like absorber thickness, shunt and series resistance, temperature, capacitance, Mott–Schottky characteristics, recombination and generation rates, current density–voltage ($J–V$), and quantum efficiency are also analyzed. The simulation demonstrates that the optimal output parameters (V_{OC}, J_{SC}, FF, and PCE) for the WS$_2$ ETL based device are 0.720 V, 45.287 mA cm^{-2}, 81.02%, and 26.45%. It is the most detailed investigation with the highest reported efficiency, significantly higher than previous research work. Using this extensive simulation study, researchers will be able to create Perovskite Solar Cells (PSCs) that are both affordable and effective while also expanding the possibilities for solar technology.

1 Introduction

The increasing reliance on conventional energy resources and the repeated depletion of fossil fuels, resulting from intense industrial activities, reveals the urgent environmental and economic challenges of today.[1–5] The conventional method of generating electricity with fossil fuels is frequently seen as unsustainable over time due to the limited availability of these resources and the environmental problems resulting from their emissions.[6] Environmental concerns have led several related organizations to promote extensive research on technologically advanced, sustainable power facilities. The substitution of fossil fuels with sustainable energy alternatives is a fundamental goal of science and technology. Solar energy is the most suitable solution to this challenge because it has the capability to meet global energy demand. Solar cells may be an effective method for converting the sun's plentiful energy into productive, low-cost, and environmentally friendly electric power.[7,8]

In regard to power conversion efficiency (PCE), research into perovskite photovoltaic (PV) technology has demonstrated significant potential as an economical substitute for silicon (Si)-based solar cell technology. As a significant advancement in third-generation solar cells, perovskite solar cells (PSCs) have a photoelectronic conversion efficiency (PCE) of 25.7%, which is equivalent to that of silicon-based models.[9–11] The remarkable photophysical and optical characteristics of perovskite material have been widely studied,[11–14] together with collective efforts to improve interfacial engineering methods, optimize materials, and fine-tune device architecture,[15–20] all of which have contributed to the significant rise in Power Conversion Efficiency (PCE). Generally, lead-based PSCs produce higher efficiency.[21–25] However, lead-based cells face performance challenges in the presence of moisture and light, and lead poisoning also poses a serious hurdle to commercialization.[26–28] For this reason, initiatives to investigate stable, lead-free perovskite compounds with effective photovoltaic performance are continuing.

[a]Materials Research and Simulation Lab, Department of Electrical and Electronic Engineering, International Islamic University Chittagong, Kumira, Chittagong, 4318, Bangladesh. E-mail: rashel.eee13@gmail.com; zahidhasan.02@gmail.com

[b]Department of Electrical and Electronic Engineering, International Islamic University Chittagong, Kumira, Chittagong, 4318, Bangladesh

[c]Department of Physics, College of Science, King Khalid University, P O Box 9004, Abha, Saudi Arabia

[d]Faculty of Engineering, Kitami Institute of Technology, 165 Kouen-cho, Kitami, Hokkaido 090-8507, Japan

Perovskite oxide, commonly known as ABO$_3$, has been intensively explored due to its unique geometry and physics.[29–31] Perovskites with matching positive and negative charges are regarded as optimal perovskite compounds. However, perovskite compounds exhibit ferroelectricity due to their non-linear positive and negative charge centers, resulting in a net dipole moment.[32] Moreover, investigations into these substances have unveiled a group of closely associated and advanced materials known as double perovskites. Double perovskite materials were discovered in the 1950s[33] and are symbolized by the formula A$_2$BB'O$_6$, with A representing alkaline earth and alkali metals, and B and B' representing transition, alkaline or alkali metals.[33,34] These double perovskite materials are highly coveted for integration into heterostructures for perovskite solar cells (PSCs), particularly for their application in absorbent layers.

Among various double perovskite structures, Cs$_2$AgBiX$_6$ (where X is Cl, Br, or I) has been extensively studied, while La$_2$NiMnO$_6$ systems have also earned significant attention, particularly for their application in perovskite solar cells.[32,35] Recent studies, such as those by Hossain *et al.*,[32] have highlighted key insights into the design of La$_2$NiMnO$_6$-based devices, focusing on different charge transport layers and utilizing DFT and SCAPS-1D frameworks for performance optimization. These investigations emphasize the material's promising photovoltaic properties and potential for enhancing power conversion efficiency. Sheikh *et al.*[36] discovered a lead-free inorganic double perovskite material, Ln$_2$NiMnO$_6$ (where Ln stands for La, Dy, Eu and Du), with a narrow band-gap range of 1.08 eV to 1.19 eV. All things considered, the materials' narrow band gap, ability to be deposited *via* chemical solutions, and high dielectric constant make them appealing for photovoltaic research.[36]

The experimental results of this study have shown commendable device performance for La$_2$NiMnO$_6$ (LNMO), Eu$_2$NiMnO$_6$ (ENMO), and Dy$_2$NiMnO$_6$ (DNMO) -based solar cells due to their optimized material properties and improved efficiency in terms of key parameters such as open-circuit voltage (V_{OC}), current density (J_{SC}), fill factor (FF), and power conversion efficiency (PCE).[36] The efficiency and performance of perovskite solar cells (PSCs) are enhanced using appropriate electron and hole-transport layers. Eu$_2$NiMnO$_6$ (ENMO) is a superior perovskite material compared to others due to its lead-free structure, non-toxic nature, and its potential for eco-friendly applications. When compared with other rare-earth compounds, ENMO has a smaller band gap.[36] These properties make it a promising candidate for photovoltaic research, as it can absorb a wide range of light, be deposited from solution, and has a high dielectric constant. The ETL is a vital component of PSCs, performing the dual function of removing electrons from the absorber and obstructing holes.[37] Conversely, the HTL affects the manufacturing cost, stability, and efficiency of solar devices.[38] Primary considerations in choosing an HTL for PSCs include the valence band offset with the absorber, hole mobility, and the associated cost,[39] whereas the ETL needs to possess a conduction band offset between the absorber and ETL that is suitable for maintaining compatibility with the high electron mobility of other layers, while also being cost-

effective.[39] An effective transfer of charge carriers produced by light from the absorber to their designated contacts in PSCs is greatly influenced by ETL and HTL. Moreover, they prevent electrons and holes from moving toward their respective electrodes. As a result, it prevents charge recombination at the ETL/absorber and absorber/HTL interfaces. Meanwhile, it separates and directs the electrically charged particles to their specified sites of contact for collection.[40]

The present work examines the effectiveness of lead-free Eu$_2$NiMnO$_6$ PSCs utilizing the SCAPS-1D framework and various ETLs and HTLs for the first time. Throughout the investigation, the performance is assessed using WS$_2$, PCBM, and C$_{60}$ as ETLs, and CFTS as the HTL, with gold (Au) employed as the back-metal contact. Furthermore, we examined the performance of the HTL and ETL layers, as well as the influence of the absorber and ETL thickness, J–V curves, generation and recombination rates, operational temperature, series resistance, shunt resistance, capacitance, Mott–Schottky analysis, and quantum efficiency.

As a double perovskite oxide, Eu$_2$NiMnO$_6$ (ENMO) is a promising alternative to lead-based perovskites because of its suitable bandgap, high stability, and environmental safety. Although ENMO has not yet been widely tested in solar cells, its successful synthesis has been reported using common oxide deposition methods. For example, sol–gel and solvothermal techniques have been used to produce ENMO with good structural quality and controlled composition.[41] In addition, pulsed laser deposition (PLD) is a well-established method for preparing high-quality oxide thin films, such as EuO, NiO, and MnO, and can also be applied to ENMO.[42] Similarly, spray pyrolysis has been demonstrated for making uniform oxide thin films, including Eu-doped TiO$_2$, and is recognized as a simple and scalable deposition technique.[43] Together, these methods show that ENMO can be prepared with reliable thin-film quality and could be integrated into stable, lead-free photovoltaic devices.

2 Numerical simulations

2.1. Numerical analysis using SCAPS-1D

The SCAPS-1D simulator was used within the computational model framework, applying Poisson's equation (eqn (1)) and continuity equations for holes (eqn (2)) and electrons (eqn (3)) to derive the photovoltaic parameters of the PSCs.[44–50] For the purpose of calculating the PV parameters, the simulation algorithm additionally accounts for loss processes using the Shockley–Read–Hall (SRH) recombination.[51,52] The symbols used in eqn (1)–(3) are as follows.[53]

$$\frac{d^2}{dx^2}\psi(x) = \frac{q}{\varepsilon_0 \varepsilon_r}\left[p(x) - n(x) + N_D - N_A + \rho_p - \rho_n\right] \quad (1)$$

For this case, the electronic potential is represented by ψ, the relative permittivity by ε_r, the permittivity of free space by ε_0, the densities of ionized donors and acceptors by N_D and N_a, the electron and hole densities by n and p, the distributions of electrons and holes by ρ_p and ρ_n, and e is the electronic charge.

$$\left(-\frac{1}{q}\right)\frac{\partial J_p}{\partial x} - U_p + G = \frac{\partial p}{\partial t} \tag{2}$$

$$\left(-\frac{1}{q}\right)\frac{\partial J_n}{\partial x} - U_n + G = \frac{\partial n}{\partial t} \tag{3}$$

According to eqn (2) and (3), J_n and J_p denote the electron and hole current densities, respectively. U_n and U_p refer to the net recombination rates for electrons and holes, and G represents the generation rate.

The overall current density, which is influenced by both concentration gradients and electric fields, can be determined by applying the drift and diffusion current formulas, as described in eqn (4) and (5).[54]

$$J_n = qn\mu_n E + qD_n\nabla n \tag{4}$$

$$J_P = qp\mu_p E - qD_P\nabla p \tag{5}$$

Here, D_n and D_P refer to the diffusion coefficients for electrons and holes. Moreover, the film's absorption constant was calculated using the new E_g-sqrt model, a revised form of the standard sqrt $(h\upsilon - E_g)$ model. The correlation between these variables is shown by eqn (6),[53] which follows the "Tauc laws".

$$\alpha(h\upsilon) = \left(\alpha_0 + \beta_0\frac{E_g}{h\upsilon}\right)\sqrt{\frac{h\upsilon}{E_g} - 1} \tag{6}$$

The photon energy is represented by $h\upsilon$, the bandgap by E_g, and the absorption coefficient by. Eqn (7) and (8) (ref. 53) provided below establishes the relationship between the model constants α_0 and β_o and the traditional constants A and B:

$$\alpha_0 = A\sqrt{E_g} \tag{7}$$

$$\beta_0 = \frac{B}{\sqrt{E_g}} \tag{8}$$

Fig. 1 outlines the SCAPS-1D simulation process in six key steps. It begins by launching the software, followed by identifying the research problem. The subsequent step involves setting the device's material properties and simulation conditions. The specific outputs to be calculated—such as J–V curves or QE—are then defined. Once configured, the simulation is initiated. Finally, the results are visualized and analyzed through simulated output curves to gain insights into device performance.

2.2. Device structure of Eu$_2$NiMnO$_6$

The layout of the optimized SC is outlined in Fig. 2(a). In this analysis, the Perovskite, along with the HTL, is chosen as the p-region, while the ETL functions as the n-region in Eu$_2$NiMnO$_6$-based devices. In this device setup, CFTS was used as the HTL, indium-doped tin oxide (ITO) for the front contact, Au as the back-metal contact (BMC), and WS$_2$, C$_{60}$, and PCBM as the ETL, with ENMO serving as the absorber layer. Eu$_2$NiMnO$_6$ crystallizes in a monoclinic double perovskite structure (space group $(P2_1/n)$), with ordered Ni^{2+}/Mn^{4+} at the B-sites and a narrow band gap near 1.1 eV—attributes highly favorable for photovoltaic absorption.[55,56] The material exhibits a high value of the room temperature, a relatively high dielectric constant ($\varepsilon\square \approx$ 300 at $\sim$50 kHz experimentally, and $\sim$6.3 from DFT), which serves to reduce recombination, and extend carrier diffusion length.[36,55,56] Furthermore, the monoclinic symmetry and optimized Ni–O–Mn bond lengths enhance orbital overlap and super exchange interactions, improving charge transport and carrier lifetime.[57] Moreover, the robust oxide perovskite framework offers enhanced chemical and thermal stability compared with halide perovskites, making Eu$_2$NiMnO$_6$ a highly attractive absorber material for solar cells. Fig. 2(a) presents the schematic construction of the main device, and Fig. 2(b) displays the ITO/ETL (WS$_2$, C$_{60}$, PCBM)/ENMO/CFTS/Au device's energy band alignment. ITO/WS$_2$/ENMO/CFTS/Au was determined to be the best computationally effective SC among all configurations. Table 1. contains the simulation's parameters for the absorber, ETLs, HTL, and front contact. Additionally, the interfacial defect layers' input parameters are given in Table 2. As the temperature is 300 K and the frequency is 1 MHz, A 1000 W m^{-2} power density characteristic of the AM1.5 G solar spectrum has been employed for all the simulations.

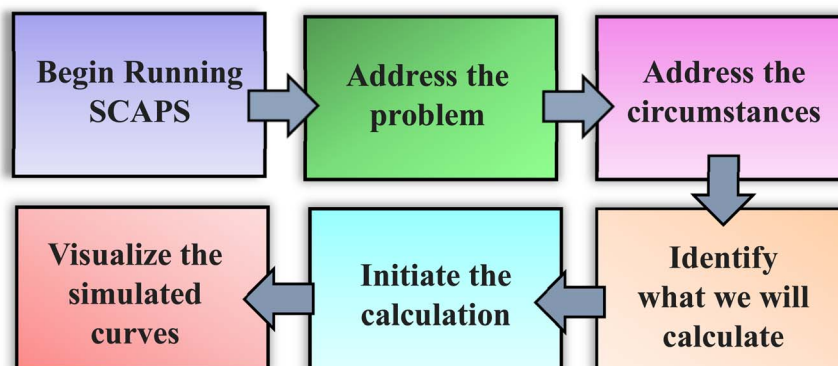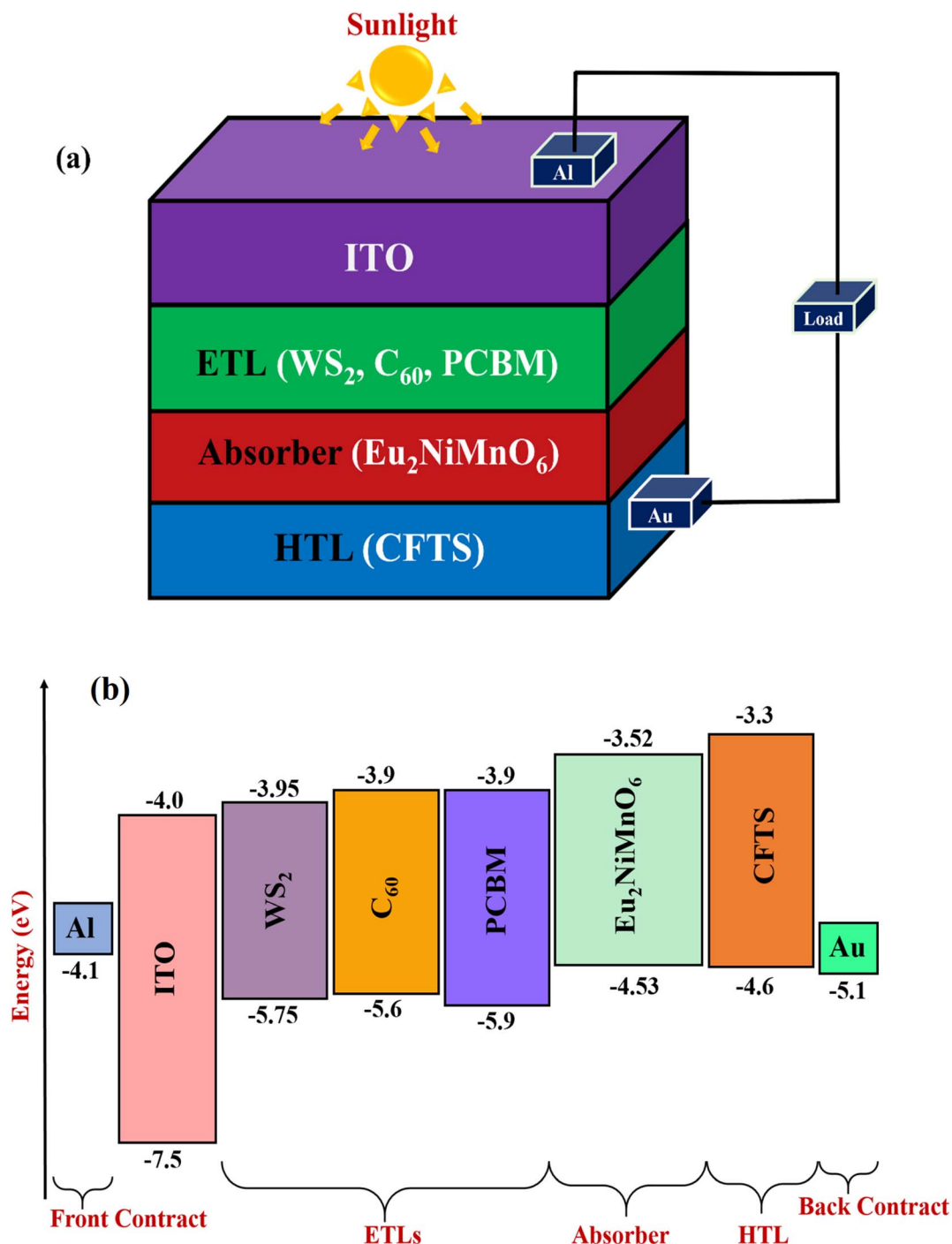**Fig. 1** Workflow for SCAPS-1D.

Fig. 2   (a) Device layout of the Eu_2NiMnO_6 – based Perovskite solar cell, (b) energy band alignment of various ETL and HTL materials with Eu_2NiMnO_6 absorber.

2.3.   Band alignment of Eu_2NiMnO_6 based solar cell

Fig. 2(b). shows a variety of solar cell structures, each employing different types of ETL, HTL, absorbers, and front and back contact materials. An exhaustive analysis of three ETLs and one HTL was conducted in our research. Analyzing various combinations in the ITO/ETL/Eu_2NiMnO_6/HTL/Au structure identifies the optimal theoretical configuration for the Eu_2NiMnO_6 (ENMO) absorber layer, as shown in Fig. 2(b). Our findings,

illustrated in Fig. 2(b) demonstrates that WS_2, which has an energy gap of 1.8 eV, provided superior performance as an ETL in conjunction with CFTS HTL in double perovskite ENMO devices. For optimal performance, the front electrode at the incident light plane needs to provide both high transmittance and superior electrical conductivity. Metal materials, including Au, are commonly used to compose the back electrode. The device's stability and efficiency can be improved by utilizing

Table 1 Input data for ITO, ETL, HTL, and absorber layers used in this work

Parameters (unit)	ITO[32]	WS$_2$ (ref. 32)	C$_{60}$ (ref. 32)	PCBM[32]	Eu$_2$NiMnO$_6$ (ref. 41 and 62)	CFTS[32]
Thickness (μm)	0.5	0.1	0.05	0.05	0.8	0.1
Bandgap, E_g (eV)	3.5	1.8	1.7	2	1.01	1.3
E_A (eV)	4	3.95	3.9	3.9	3.52	3.3
ε_r	9	13.6	4.2	3.9	9	9
N_C (cm^{-3})	2.2×10^{18}	1×10^{18}	8×10^{19}	2.5×10^{21}	1×10^{18}	2.2×10^{18}
N_V (cm^{-3})	1.8×10^{19}	2.4×10^{19}	8×10^{19}	2.5×10^{21}	1×10^{18}	1.8×10^{19}
Electron thermal velocity (cm s^{-1})	1×10^7	1×10^7	1×10^7	1×10^7	1×10^7	1×10^7
Hole thermal velocity (cm s^{-1})	1×10^7	1×10^7	1×10^7	1×10^7	1×10^7	1×10^7
μ_n (cm^2 V^{-1} s^{-1})	20	100	8×10^{-2}	0.2	22	21.98
μ_h (cm^2 V^{-1} s^{-1})	10	100	3.5×10^{-3}	0.2	22	21.98
N_D (cm^{-3})	1×10^{21}	1×10^{18}	1×10^{17}	2.93×10^{17}	0	0
N_A (cm^{-3})	0	0	0	0	7×10^{16}	1×10^{18}
N_t (cm^{-3})	1×10^{15}	1×10^{15}	1×10^{15}	1×10^{15}	1×10^{15}	1×10^{15}

a high-quality back electrode, which also helps with carrier collection.[58] The Au electrode (WF ~5.1 eV) is deemed the most suitable for most Eu$_2$NiMnO$_6$ PSCs because of their mesoporous or planar structure, as depicted in Fig. 2(b). The performance gain observed in Fig. 2(b) arises from the favorable energy alignment of WS$_2$ with the absorber. Specifically, WS$_2$ introduces a small positive conduction band offset (CBO, −0.43 eV), which forms a moderate spike at the ETL/absorber interface. Such alignment is beneficial because it suppresses interfacial recombination by raising the barrier for electron back-transfer, while still allowing efficient electron extraction. Previous SCAPS-based studies have shown that this CBO within the optimal range significantly enhances device performance, whereas negative offsets ("cliffs") lead to increased recombination losses, and excessively large spikes (>0.5 eV) can obstruct electron transport[59,60] Similarly, the valence band offset (VBO) at the absorber/HTL interface plays a complementary role: a moderate positive VBO (+0.07 eV) ensures selective hole extraction while blocking electron leakage, thereby reducing recombination and maintaining high device efficiency. In consideration of these findings, the favorable CBO of WS$_2$ and an optimized VBO enable efficient charge carrier separation, suppression of recombination, and enhanced photovoltaic performance, consistent with earlier SCAPS modeling reports.[61]

3 Result & discussion

3.1. Influence of VBO and CBO

Exposure of the solar cell to sunlight generates electrons and holes within the perovskite absorber layer. The conduction and valence band offsets (CBO and VBO) at the interfaces of ETL/

absorber and absorber/HTL primarily dictate the efficiency of separating charge carriers.[63] These offsets directly influence the device's performance.

The CBO for the ETL/absorber interface is expressed as.[64]

$$CBO = X_{Absorber} - X_{ETL} \tag{9}$$

In the preceding instance, $X_{Absorber}$ and X_{ETL} stand for the absorber's and ETL's electron affinities, subsequently, while CBO stands for conduction band offsets.

Three distinct barrier types are observed at the ETL/absorber interface: virtually flat, cliff-like, and spike-like.[65] A negative CBO forms as a cliff-like barrier when X_{ETL} exceeds $X_{Absorber}$. This implies that the ETL possesses a lower conduction band minimum (CBM) compared to the absorber. In the absence of a CBO, a flat barrier results in no energy differences and, as a result, no barrier to charge transfer.

On the other hand, when ETL's CBM exceeds the absorber's ($X_{ETL} < X_{Absorber}$), a positive CBO corresponds to the appearance of a spike-like barrier. The VBO shown in Table 3 at the contact between the absorber and the HTL is defined as.[64]

$$VBO = X_{HTL} - X_{Absorber} + E_{g,HTL} - E_{g,Absorber} \tag{10}$$

Table 3 Provides the VBO and CBO values for each ETL

Absorber	ETLs	CBO	VBO
Eu$_2$NiMnO$_6$	WS$_2$	−0.43	0.07
	C$_{60}$	−0.38	0.07
	PCBM	−0.38	0.07

Table 2 Data for interface parameters used in the Eu$_2$NiMnO$_6$-based solar cell[32]

Interface	Defect type	Capture cross section: electrons/holes (cm^2)	Energetic distribution	Reference for defect energy levels, E_t	Interface defect density (cm^{-2})
ETL/Eu$_2$NiMnO$_6$	Neutral	1×10^{-17} 1×10^{-18}	Single	Above the VB maximum	1×10^{10}
Eu$_2$NiMnO$_6$/HTL	Neutral	1×10^{-18} 1×10^{-19}	Single	Above the VB maximum	1×10^{10}

In this context, VBO represents Valence Band Offsets, X_{HTL} HTL indicates the electron affinity of the HTL, and $E_{g,HTL}$ and $E_{g,Absorber}$ denotes the bandgaps of the HTL and absorber.

The calculations for CBO and VBO were performed with eqn (9) and (10).[64] The CBO, as well as the VBO for WS_2 is:

The CBO at the ETL/absorber interface is defined as = $X_{Absorber} - X_{ETL} = 3.52 - 3.95 = -0.43$ eV. In this instance, the CBO is negative, and the nature of the barrier is cliff-like.

The VBO at the absorber/HTL interface is defined as = $X_{HTL} - X_{Absorber} + E_{g,HTL} - E_{g,Absorber} = 3.3 - 3.52 + 1.3 - 1.01 = 0.07$ eV. Here, there is a spike-like barrier that has a positive CBO. We can also determine the CBO and VBO of other ETLs in a similar way as presented in Table 3.

3.2. Band diagram

Fig. 3(a–c) displays the optimized Eu_2NiMnO_6(ENMO)-based PSCs' energy band diagrams. The Electron affinity of the ETL has to be greater than that of the ENMO in order to transfer the electron to the absorber-ETL interface, and the ionization energy has to be lower than that of the Eu_2NiMnO_6 (ENMO) in order to close the gaps in the material's contact. Energy level alignment has a major impact on the efficiency and performance of PSCs. WS_2, C_{60}, and PCBM ETLs have bandgaps of 1.8, 1.7, and 2 eV, accordingly, their performances with the same heterostructure are very similar to each other. The variation in energy levels among WS_2, C_{60}, and PCBM arises from differences in their electron affinities and band gaps, which influence how their conduction bands align with the ENMO absorber. WS_2, with an electron affinity of 3.95 eV and a bandgap of 1.8 eV, creates a conduction band offset of -0.43 eV, promoting efficient electron extraction but potentially increasing interfacial recombination. C_{60} and PCBM, with slightly lower electron affinities ($\sim$3.90 eV), generate smaller offsets (-0.38 eV), which reduce recombination risk but may slightly limit carrier transfer. PCBM's wider bandgap also improves hole blocking at the interface. These differences in band alignment directly affect carrier transport and device efficiency, helping to explain why WS_2-based cells achieved the highest performance in our simulations.[66,67] In general, the thickness of C_{60} and PCBM layers is typically less than 100 nm.[68] However, in this theoretical study, we observed that when the thickness of WS_2 is set to 50 nm, the efficiency is significantly lower than when a 100 nm thickness is used. Therefore, to achieve better performance and more accurate results, we have chosen to use a WS_2 thickness of 100 nm for this investigation. In Fig. 3(a–c), the quasi-Fermi levels F_n and F_p are aligned with the valence band energy of each device. Both the conduction band's (E_C) and valence band's (E_V) energy, accordingly. For each ETL, F_p was positioned over the E_V, while F_n and E_C kept up their harmonically similar operations.

3.3. Influence of absorber and ETL thickness on the performance of solar cells

The thickness of both the ETL and absorber layers plays a crucial role in enhancing the PV output features of the SCs. To accomplish the best-performing solar collectors, PV outputs
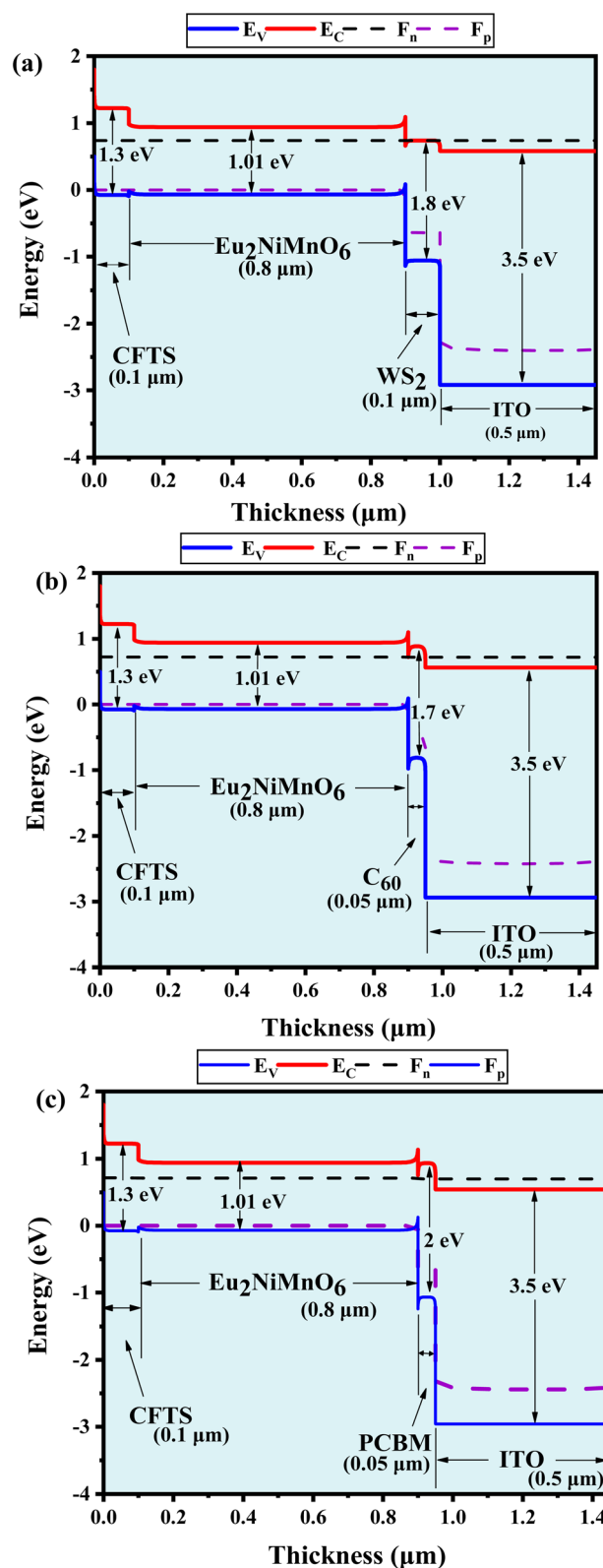

Fig. 3 Energy band diagrams for (a) WS_2, (b) C_{60}, and (c) PCBM.

must be optimized.[32] To attain maximum efficiency in SCs, optimizing the performance of photovoltaic (PV) systems is necessary.[32] The first and most important stage of creating high-

performance SCs is selecting the appropriate absorber, ETL, and HTL combination. During this analysis, we selected WS$_2$, C$_{60}$, and PCBM as ETL, Eu$_2$NiMnO$_6$ as an absorber, and CFTS as HTL. Contour maps for V_{OC}, J_{SC}, FF, and PCE of Eu$_2$NiMnO$_6$ (ENMO)-based PSCs are shown in Fig. (4–7), with variations plotted against absorber and ETL thickness of (0.4–1.2) and (0.025–0.125) μm. The thickness of both the absorber and ETL strongly affects the rates of carrier generation and recombination in the device. A thicker absorber allows more photons to be
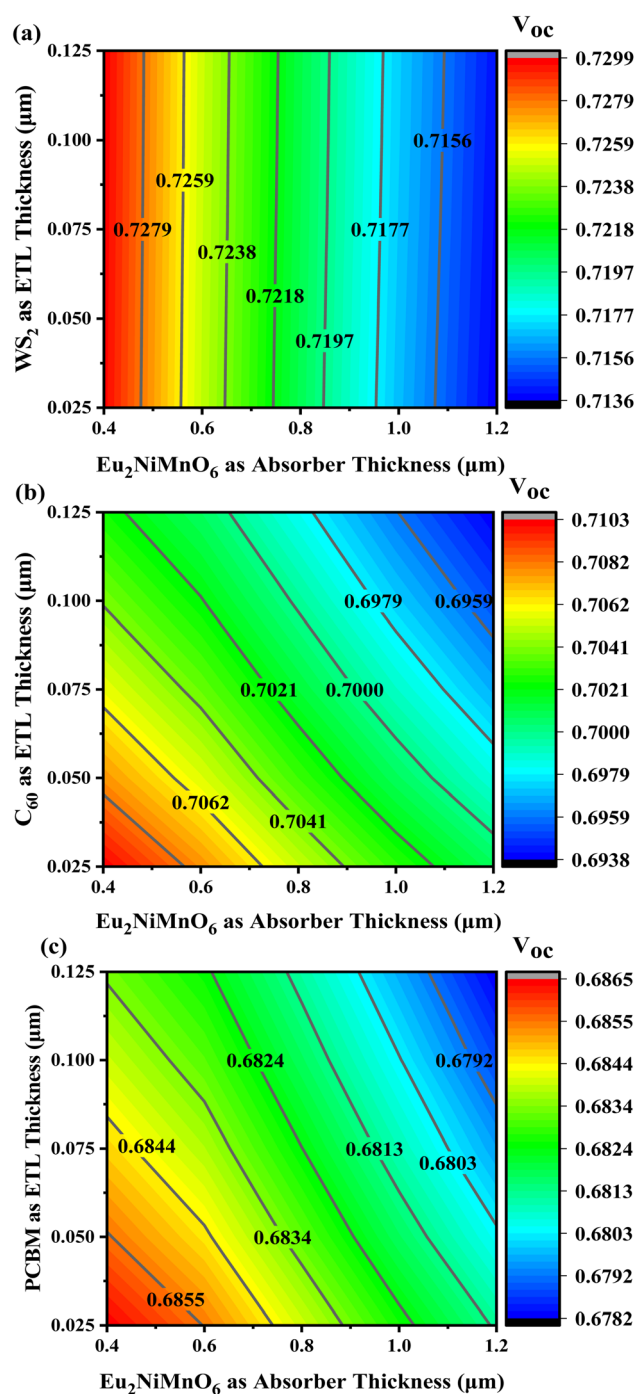

Fig. 4 Contour mapping of V_{OC} shows effects of varying ETL and absorber thicknesses for ETLs including (a) WS$_2$, (b) C$_{60}$, and (c) PCBM.
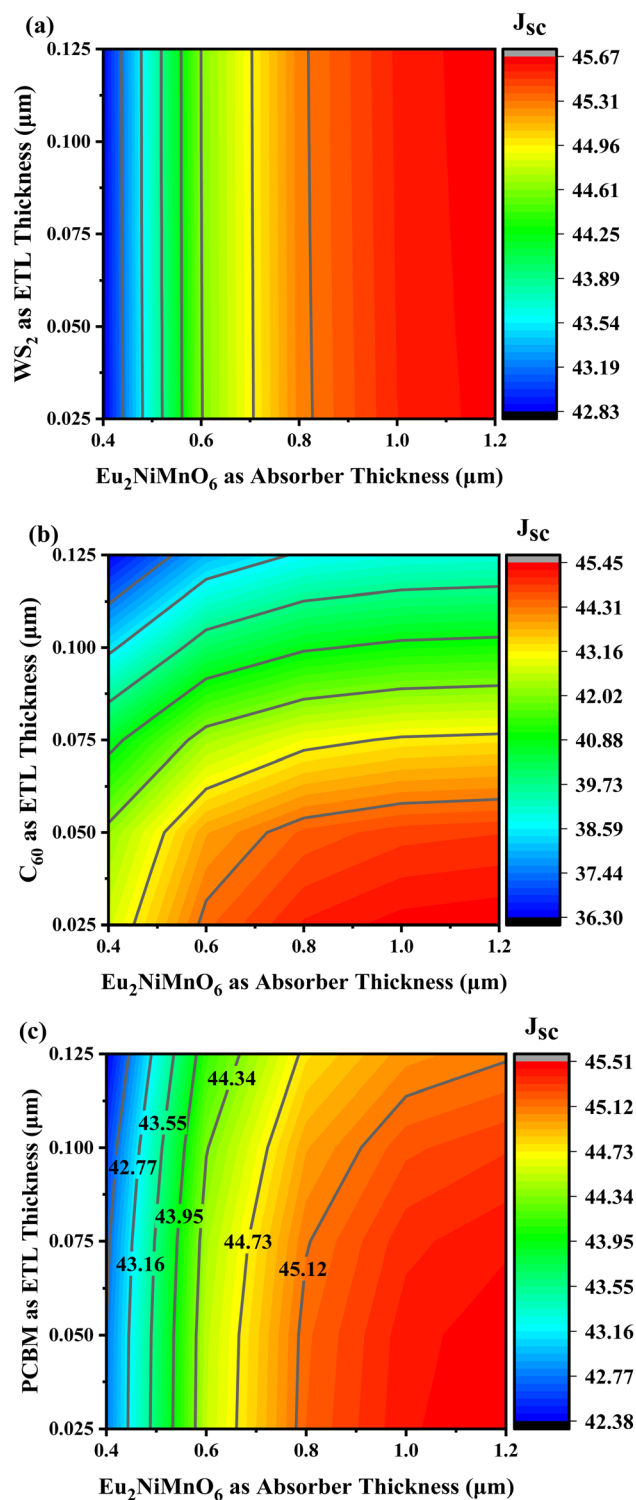

Fig. 5 Contour mapping of J_{SC} shows effects of varying ETL and absorber thicknesses for ETLs including (a) WS$_2$, (b) C$_{60}$, and (c) PCBM.

absorbed, which increases the number of electron–hole pairs generated. However, when the absorber becomes too thick, carriers generated deep inside face longer transport paths, which increases bulk recombination before they reach the junction.[66,69] On the other hand, the ETL thickness mainly controls charge extraction and interfacial recombination. An
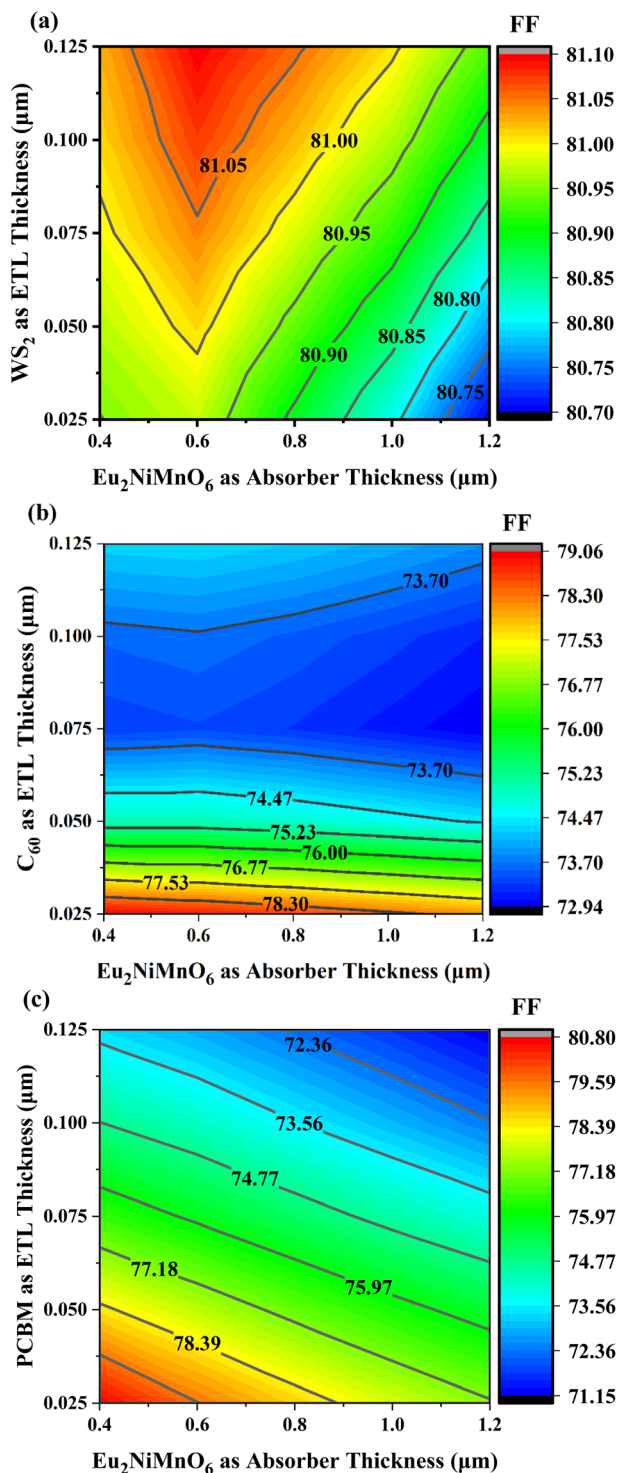
Fig. 6 Contour mapping of FF shows effects of varying ETL and absorber thicknesses for ETLs including (a) WS$_2$, (b) C$_{60}$, and (c) PCBM.

Fig. 7 Contour mapping of PCE shows effects of varying ETL and absorber thicknesses for ETLs including (a) WS$_2$, (b) C$_{60}$, and (c) PCBM.

ETL that is too thin may not effectively block holes, leading to interfacial recombination, while an excessively thick ETL increases resistance to electron transport, which also promotes recombination losses.[70–72] Therefore, as shown in Fig. 7, the contour mapping of PCE reflects a balance: sufficient absorber thickness is need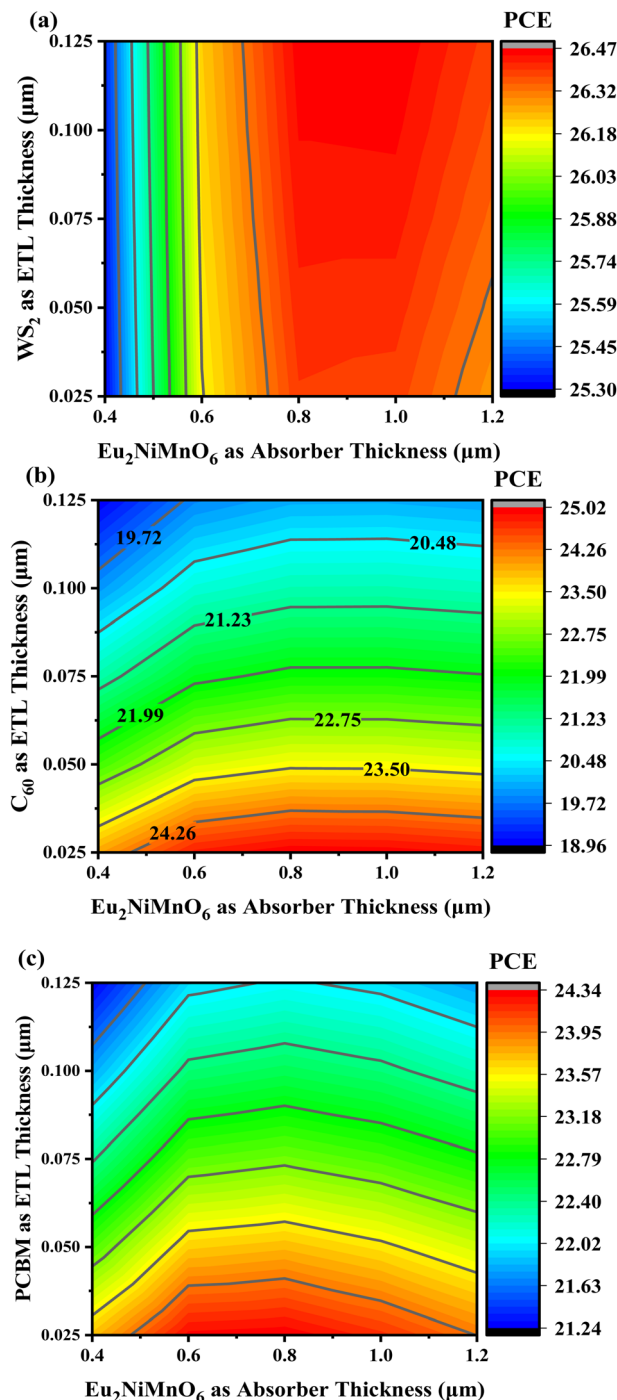ed for maximum carrier generation, while optimized ETL thickness ensures efficient extraction and minimal recombination.

The contour plots in Fig. 4(a–c) demonstrate the effect of altering both ENMO absorber layer and ETL thickness on the open-circuit voltage (V_{OC}) of the solar cells. According to Fig. 4(a), V_{OC} levels reached their maximum at ETL thicknesses of 0.025–0.125 μm and absorber thicknesses of around 0.4–0.45 μm. Compared to all other structures, the ITO/WS$_2$/ENMO/CFTS/Au PSC structure recorded the highest V_{OC} value of

0.7299 V. Out of all the PSCs under study, the ETL of 0.025–0.50 μm and absorber of 0.4–0.6 μm is the optimum thickness range to obtain best V_{OC} ~0.71 V for ITO/C$_{60}$/ENMO/CFTS/Au device and The PCBM ETL registered the lowest V_{OC}, which was 0.6865 V, its absorber thickness was between 0.4-0.55 μm and ETL thickness between 0.025-0.037 μm, according to Fig. 4(c). Since V_{OC} increased as the ETL layer's thickness reduced, as graph Fig. 4(a–c) illustrates. It happens due to, enhanced absorber layer thickness results in increased carrier recombination rates, which raise the saturation current affecting the photocurrent.[32]

Fig. 5 illustrates the different thicknesses of the ENMO and ETL layers in the tested SC setups impact J_{SC}. Fig. 5(a) demonstrates WS$_2$ as ETL in the configuration, featuring absorber and ETL thicknesses near (0.95–1.2) μm and (0.025–0.125) μm, accordingly, resulting in a greater J_{SC} value of 45.67 mA cm^{-2}. Observations were made when the absorber and ETL thicknesses were around (0.9–1.2) and (0.025–0.095) μm. A J_{SC} of 45.51 mA cm^{-2} was achieved with PCBM as ETL. The minimum J_{SC} value of 45.45 mA cm^{-2} was found when C$_{60}$ as ETL. The spectral response at longer wavelengths causes the J_{SC} values for each SC to go up as the thickness of the absorber grows, whereas partial light absorption causes the J_{SC} values to drop with an increase in ETL thickness.[73]

The variations in FF are driven by the interplay of material properties, energy level alignment, charge extraction efficiency, and interface quality.[74,75] The contour diagrams in Fig. 6 exhibit the FF changes when the absorber and ETL thickness are changed. Fig. 6(a) shows that the WS$_2$ ETL-based device had an FF of 81.10%, which is the highest among these three SC configurations for absorber and ETL thicknesses of nearly 0.52–0.68 μm and 0.1–0.0125 μm. While the PCBM-based ETL device had an FF of 80.80% with absorber and ETL thicknesses of around 0.4–0.55 μm and 0.01–0.037 μm, respectively, and among the ETLs, C$_{60}$ had the lowest FF, recorded at 79.06%. WS$_2$ outperforms PCBM and C$_{60}$ due to its superior electronic properties, better energy alignment, and lower recombination losses, while the impact of ETL thickness remains minimal in these configurations.[76] Interestingly, ETL thickness is not a major factor in maximizing the FF values, for all three different solar configurations.

The thickness of the absorber layer, which is determined by the carriers generated through photosynthesis, has been carefully optimized to the ideal level for creating a solar cell with improved efficiency.[77] Contour plots in Fig. 7 depict PCE changes due to absorber and ETL thickness variations. The solar structure WS$_2$-based-ETL, with an absorber thickness ranging from 0.75 to 1.05 μm and an ETL thickness of around 0.03 to 0.125 μm, achieved the maximum PCE among all the modified solar structures. It achieved a PCE of approximately 26.47% as shown in Fig. 7(a). Regarding the thickness of the absorber and ETL, C$_{60}$ and PCBM based ETL device exhibit a similar PCE of around 25.02% and 24.34%, respectively (Fig. 7(b and c)). Increasing the absorber thickness indicates higher efficiency because the thick absorber layers improve carrier recombination, whereas excessively thin layers cannot generate carriers efficiently, which lowers the overall device

efficiency. However, the PCBM ETL-based solar setup, with an absorber layer thickness of around 0.55–1 μm and an ETL thickness of around 0.025–0.032 μm, displays the smallest PCE of about 24.34% Fig. 7(c).

3.4. Influence of acceptor density and absorber thickness on the performance of solar cells

This study investigates the effects of absorber thickness and acceptor density (N_A) in ENMO-based SCs. The observed effect's statistical significance is presented in (Fig. 8–11). To explore the effect of these parameters on the PV performance characteristics of the three optimized PSCs throughout the simulation in Fig. 8–11, the absorber thickness was adjusted between 0.4 to 1.2 μm, and N_A varied from 7×10^{14}–7×10^{18} cm^{-3}. The influence of absorber thickness and N_A on V_{OC} is shown in Fig. 8(a–c). Fig. 8(a) illustrates that WS$_2$-based ETLs produce the largest V_{OC} of 0.7480 V. Whenever the absorb thickness is determined, it varies from 0.4 to 1.2 μm, and the N_A varies between 7×10^{17}–7×10^{18} cm^{-3}. The V_{OC} for the C$_{60}$ ETL-based structure was 0.7164 V, and for the PCBM ETL-based structure, it was 0.6912 V (Fig. 8(b and c)), with the absorber thickness from 0.4 to 1.2 μm and 0.4 to 1.2 μm and the N_A from 7×10^{17}–7×10^{18} cm^{-3} for both cases. However, it should be noted that A similar response in SC structures with ETLs was observed when the absorber thickness was adjusted by varying the N_A of WS$_2$, C$_{60}$, and PCBM.

Fig. 9 illustrates how the three enhanced SC structures under consideration's J_{SC} values vary in response to adjustments in the absorber layer's thickness and N_A. Out of these three solar configurations, the WS$_2$ ETL-based device exhibits the highest J_{SC} value, reaching 46.16 mA cm^{-2}, when N_A is approximately between a higher of 7.0×10^{14}–7.0×10^{15} cm^{-3}, and the thickness of the absorber falls between 1 to 1.2 μm Fig. 9(a). The lowest J_{SC} values are seen in C$_{60}$, an ETL-based solar structure, which is 44.98 mA cm^{-2} in cases when the absorber thickness ranges around 0.9 to 1.2 μm and the N_A value is around 7×10^{16} to 7×10^{18} cm^{-3} (Fig. 9(b)). PCBM as ETL shows J_{SC} value of 46.1 cm^{-3} during a thickness of 1–1.2 μm for the absorber, and the N_A value is around 7×10^{14}–7×10^{15} cm^{-3} (Fig. 9(c)). Remarkably, this shares a similarity with WS$_2$ (ETL).

Fig. 10(a–c) illustrates the influence of absorber thickness and N_A on FF. WS$_2$ ETL-related PSC indicates 81.10% for FF when absorber thickness is (0.4–1.2) μm and N_A is in the range from around 7×10^{15} to 7×10^{17} cm^{-3} on the basis of Fig. 10(a). C$_{60}$ (ETL)-based device displays an FF of 76.00% when absorber thickness is 0.4–1.2 μm, which is the lowest. PCBM (ETL)-associated PSC displays an FF of 81.20% when N_A varies between 7×10^{17}–7×10^{18} cm^{-3}. Moreover, with PCBM-based ETL, the greatest value of FF can be attained. The higher FF of PCBM-based PSCs compared to WS$_2$-based PSCs is due to PCBM's superior electron mobility, better energy level alignment, and more favourable interface characteristics, which reduce recombination losses and enhance charge extraction.[78] Additionally, WS$_2$ has a higher defect density, which hampers charge transport.[79] These combined factors contribute to the slightly higher FF observed in PCBM-based devices.
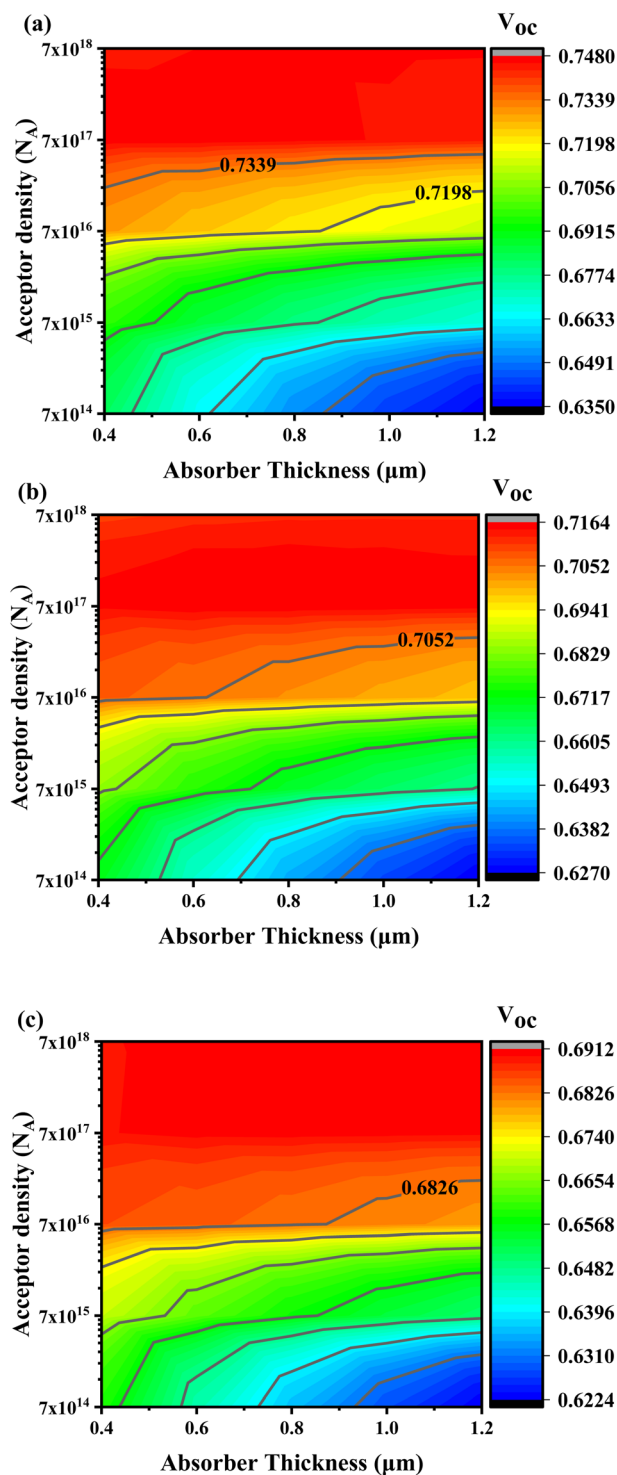
Fig. 8 Contour mapping of V_{OC} showing the effects of varying in absorber thickness and N_A for ETLs, including (a) WS$_2$, (b) C$_{60}$, and (c) PCBM.

Fig. 9 Contour mapping of J_{SC} showing the effects of varying in absorber thickness and N_A for ETLs including (a) WS$_2$, (b) C$_{60}$, and (c) PCBM.

The effects of varying absorber thickness and N_A on PCE for the three PSCs can be seen in Fig. 11(a–c). Fig. 11(a–c) illustrates that the highest PCE values for WS$_2$, C$_{60}$, and PCBM ETLs are 27%, 24.34%, and 25.35%, respectively, as the ENMO thickness is varied from 0.6 μm to 1.2 μm for WS$_2$, C$_{60}$, and PCBM. The N_A falls between 7×10^{17}–7×10^{18} cm^{-3}. Among these three, WS$_2$

(ETL) shows the maximum PCE and the C$_{60}$ based ETL configuration shows the minimum PCE.

3.5. Influence of varying absorber and HTL layer thickness on PV performance

The performance of the device was improved by raising the absorber thickness from 400 nm to 1400 nm, since it affected

Fig. 10 Contour mapping of FF showing the effects of varying in absorber thickness and N_A for ETLs including (a) WS$_2$, (b) C$_{60}$, and (c) PCBM.
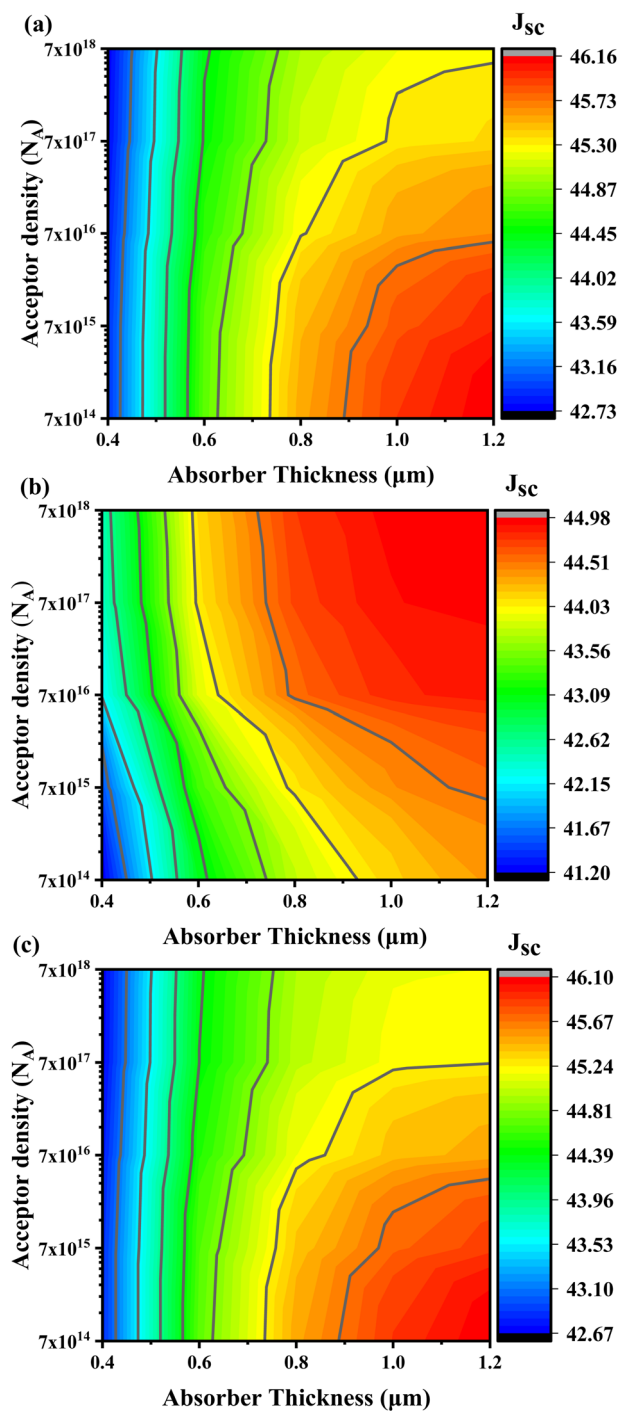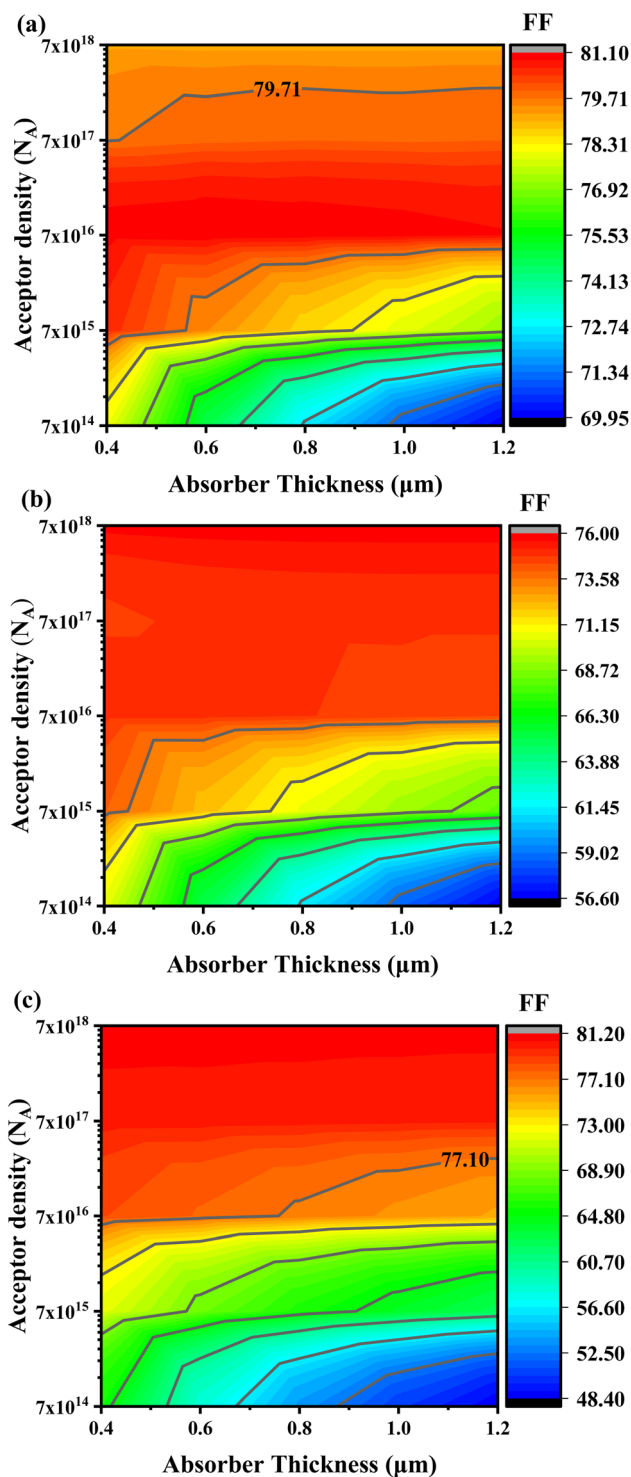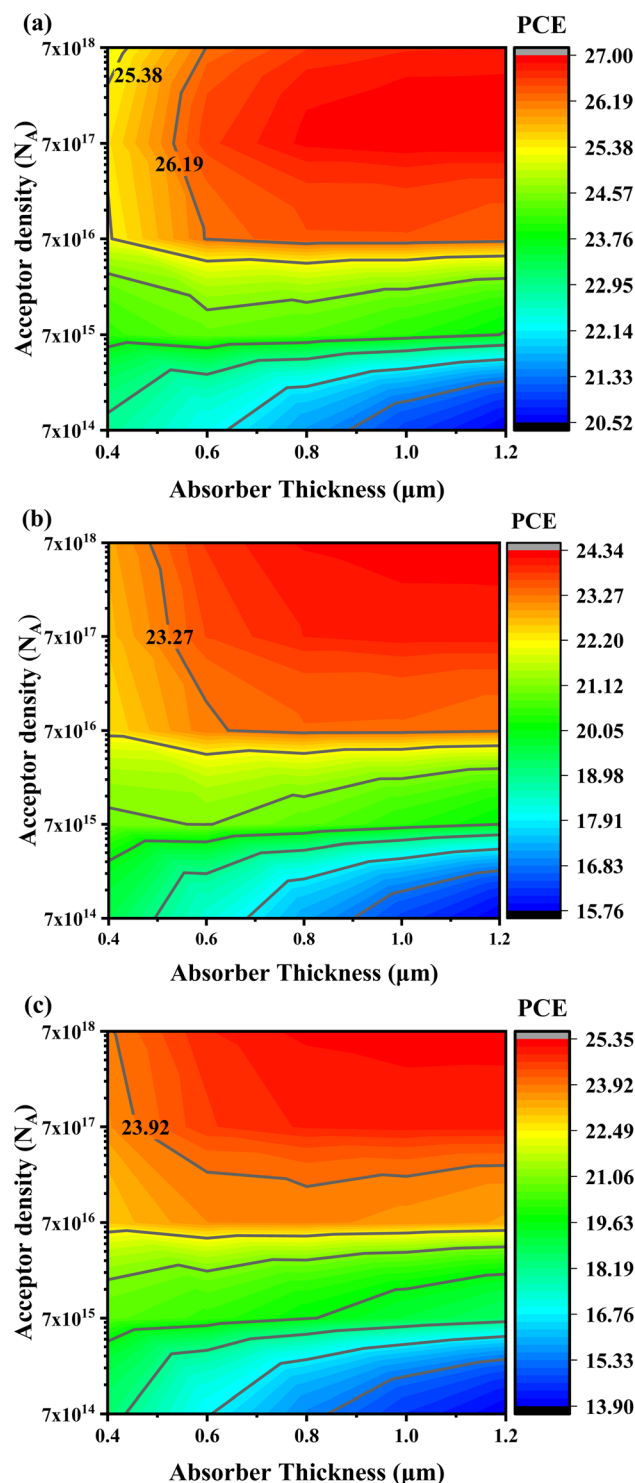

Fig. 11 Contour mapping of PCE showing the effects of varying in absorber thickness and N_A for ETLs including (a) WS$_2$, (b) C$_{60}$, and (c) PCBM.

the ITO/ETL (WS$_2$, C$_{60}$, PCBM)/ENMO/CFTS/Au structure's performance. Fig. 12(a) illustrates how the PSC's performance changes with varying absorber thickness for different ETLs. During the optimization process, higher reverse saturation current and absorber thickness caused a decrease in the PSC's

V_{OC}.[80] The WS$_2$-based ETL design exhibits the highest value of V_{OC} compared to other configurations, which is ~0.73 V, and the PCBM ETL-based device displays the smallest value of V_{OC} is ~0.68 V. In the case of J_{SC}, all three structures followed the same pattern, while C$_{60}$ ETL-based device revealed the lowest value

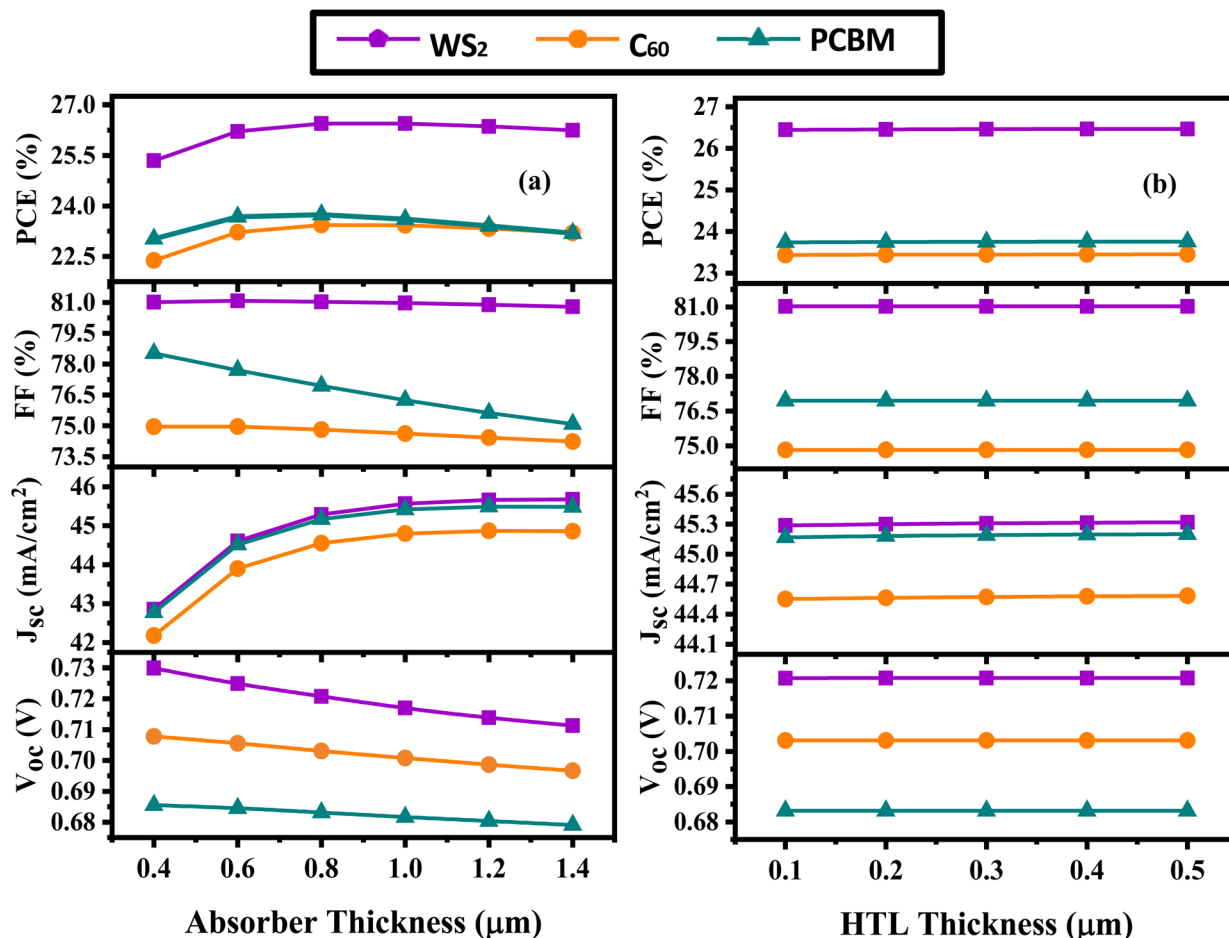**Fig. 12** Impact of varying (a) absorber thickness and (b) HTL thickness on PV parameters.

$\sim$44.5 mA cm^{-2}. However, the PCBM-based ETL structure shows a nearly linear decreasing pattern. The WS$_2$ ETL-based PSC has the greatest FF value at 81%. In terms of PCE, each configuration shows the same scenario of increasing except PCBM ETL-associated structure. The maximum efficiency is $\sim$26.3% displayed by the WS$_2$ ETL-based structure at 0.8 μm and the lowest value is $\sim$22% displayed by the C$_{60}$-based structure. Thicker absorber layers enhance carrier recombination, while very thin layers are less efficient at generating carriers, which reduces the overall device efficiency.[81] To improve V_{OC} ($\sim$0.72 V), J_{SC} ($\sim$45.5 mA cm^2), FF (81%), and PCE ($\sim$26.3%), the optimal thickness for the Eu$_2$NiMnO$_6$ absorber was determined to be 0.8 μm in the investigation.

The effect of varying CFTS HTL thickness on PV parameters is shown in Fig. 12(b). CFTS is exclusively considered the HTL in thickness optimizations due to its highest PCE, with the effect of increasing CFTS thickness shown in Fig. 12(b), suggesting that the values of PCE, FF, J_{SC}, and V_{OC} for every ETL stayed constant. The optimal HTL thickness of 0.1 μm results from a balance between efficient hole extraction, minimal series resistance, and reduced recombination at the absorber/HTL interface. When the HTL is thinner than 0.1 μm, it may not fully cover the absorber surface, which can create incomplete

contact and pathways for interfacial recombination, thereby reducing V_{OC} and FF.[66,82] On the other hand, when the HTL is thicker than 0.1 μm, holes must travel longer distances through the transport layer. This increases series resistance and reduces carrier mobility, which limits charge extraction and lowers J_{SC} and overall PCE.[71,83] In addition, an overly thick HTL can introduce additional trap states at the interface and increase the probability of recombination before carriers reach the electrode.[84] Therefore, at 0.1 μm, the HTL is thick enough to ensure complete coverage and good band alignment with the absorber, but still thin enough to minimize transport losses, giving the best trade-off in photovoltaic performance ($V_{OC} \approx 0.72$ V, $J_{SC} \approx 45.3$ mA cm^{-2}, FF $\approx 81\%$, and PCE $\approx 26.5\%$) for ITO/WS$_2$/ENMO/CFTS/Au structure. The V_{OC} value stays constant at around 0.72 V for WS$_2$, 0.70 V for C$_{60}$, and PCBM as ETLs at nearly 0.68 V for the increased thickness of CFTS. During the thickness of the CFTS improved the J_{SC} value of C$_{60}$ indicated a lower value of 44.5 mA cm^{-2}, while WS$_2$ displayed a higher value of 45.3 mA cm^{-2}. Out of all configurations, the WS$_2$-based structure achieves the best FF and PCE values, at about 81.1% and 26.5%, respectively. The C$_{60}$ ETL-associated cell provides the smallest PCE and FF value with enhanced CFTS thickness, clocking in at around 23.5% and 75%, respectively. In the

earlier study, it was noted that when the HTL thickness grew, the PCE value increased as well.[85] Regarding the change, It was found that a thickness of 0.1 μm for the HTL was optimal for achieving higher PCE, so 0.1 μm was selected to be the optimized thickness of the HTL for further examination, which was also aligned with the earlier study.[86]

3.6. Influence of temperature, shunt, and series resistance on Eu₂NiMnO₆

3.6.1 Effects of series resistance. The right and left side metal contacts, connections among the layers of the solar cell, and manufacturing flaws are the main sources of the series (R_s) and shunt (R_{sh}) resistances, which strongly influence the efficiency of solar cells.[53] The shunt resistance did not change from 10^5 Ω cm^2, the influence of R_s changed from 0 and 6 Ω cm^2, as indicated in Fig. 13(a) regarding the three (ITO/ETL/ENMO/CFTS/Au) structures. The declared figure shows that the PCE was decreasing for all three structures with a fluctuation of R_s. For the WS₂ ETL-based structure, the PCE value fell from about 26% to 17.5%. On the other hand, the PCE of structures with C₆₀ and PCBM ETLs decreased from about 23% to 15%, similar to another study of double perovskite SCs.[86] It has been seen that the PCE value of C₆₀ and PCBM ETL-based solar cells decreased similarly. For each of the three structures, the value of R_s also had an impact on the FF value. The FF value of WS₂ ETL-associated solar device decreased from around 82% to 50%.

In contrast, the FF value of C₆₀ and PCBM ETL-based devices decreased from around 75% to 48% and from 76 to 46%. The fill factor (FF) declined consistently due to the enhanced series resistance.[87] Consequently, throughout the device's manufacture, R_s must be reduced to a minimum to maximize performance and optimize FF. The J_{SC} value of WS₂ and PCBM ETL-based designs was slightly decreased with the variation of R_s, which was around 45.3 to 45.2 mA cm^{-2} for WS₂ ETL-based cells and around 45.2 to 45 mA cm^{-2} for PCBM-based cells. However, regarding the C₆₀-based structure, the J_{SC} value decreased gradually from 44.5 to 43.8 mA cm^{-2} with the variation of R_s. The V_{OC} value remained constant for all three structures with the variation of series resistance, demonstrating no impact on the V_{OC} of R_s for all three studied configurations. It is also seen in previous double Perovskite-based studies.

3.6.2 Effects of shunt resistance. The device shunt resistance (R_{sh}) is an essential internal electrical component that influences the efficiency of SCs. It considers current leakage across the donor–acceptor and active layer-electrode boundaries.[86] In our study, Fig. 13(b) represents the effects of R_{sh} in the case of three separate ETL-based SC structures. In Fig. 13(b), R_{sh} varied in ranges of 10^1 to 10^7 Ω cm^2 for all three configurations. As R_{sh} climbed, the V_{OC}, PCE, and FF readings all displayed a similar pattern except for J_{SC}. It is also seen in previous studies.[88] It was noticed that the value of V_{OC}, PCE, and FF instantly increased in the range of 10^1 to 10^2 Ω cm^2 of R_{sh} value. In the case of V_{OC}, the WS₂ ETL-associated solar configuration
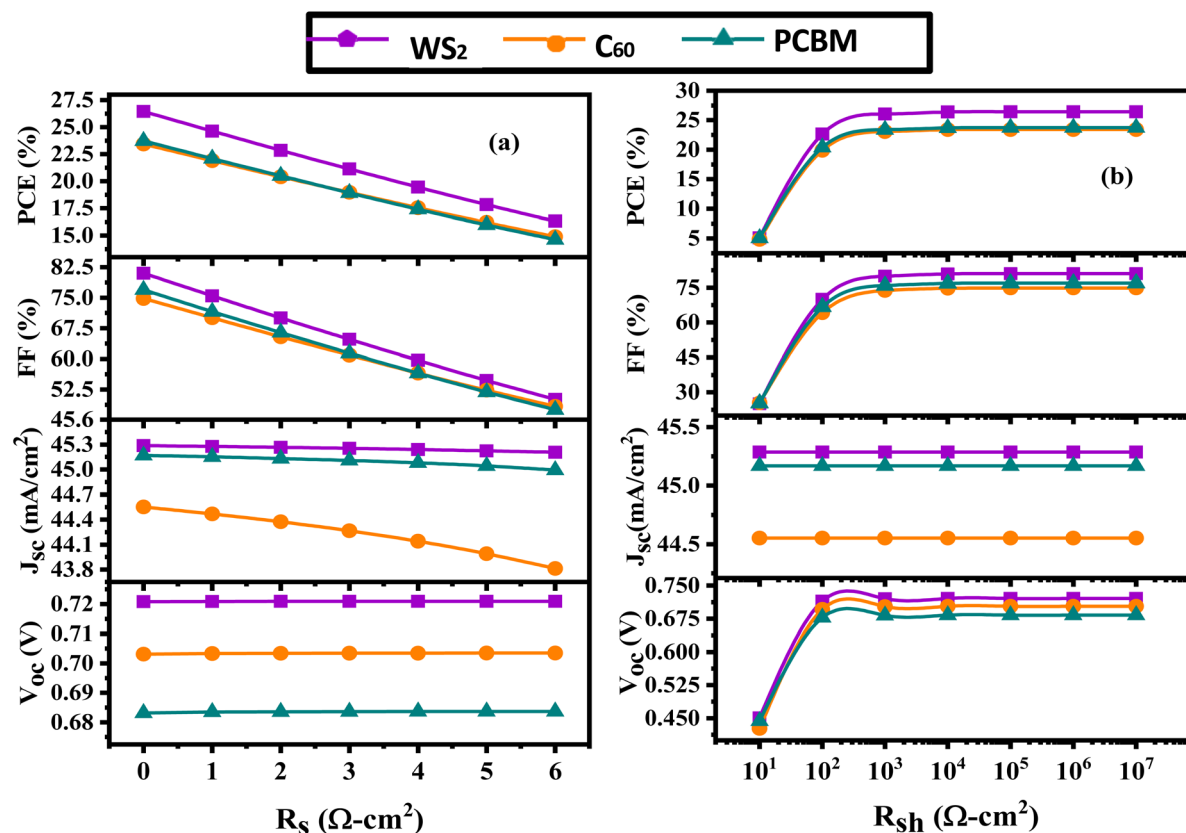

Fig. 13 Effects of (a) series resistance and (b) shunt resistance on PV parameters.

© 2025 The Author(s). Published by the Royal Society of Chemistry

displayed a maximum of ~0.71 V at an R_{sh} value around 10^2 Ω cm^2 and remained constant after 10^3 Ω cm^2. In comparison with the other PSCs, the Structures based on PCBM-ETL provided a minimum voltage of close to 0.635 V (Fig. 13(b)). The J_{SC} for all three configurations is about the same, with the C$_{60}$ ETL-based PSC displaying a minimum of around 44.5 mA cm^{-2} and the WS$_2$ ETL-associated solar structure showing a maximum of around 45.25 mA cm^{-2}. Among all the configurations, the FF of the WS$_2$ ETL-based device PSC possessed the greatest at ~81% and the C$_{60}$ ETL-associated solar cell indicated the smallest value of ~70%. In the case of PCE, the WS$_2$ ETL-based PSC illustrated the greatest value of ~25% and the remaining two PSCs C$_{60}$ and PCBM, ETL-based structure indicated almost a similar value of ~20%. Because of the fluctuation in R_{sh}, a pattern of variation was seen with the various PV parameters, which agreed with the results of the earlier investigation.[89] To achieve optimal performance for the device, it is crucial to minimize the series resistance and maximize the shunt resistance.[90]

3.6.3 Effects of temperature. An increase in temperature from (275–320) K in our investigation is shown in Fig. 14 as an effect on the device's performance characteristics. The temperature impacts for three distinct PSC setups are

illustrated in the preceding Fig. 14. At the time of changing temperature, we found variations in V_{OC}, PCE, and FF for all three configurations. In the case of PCE, all three configurations showed similar trends of declining efficiency considering the rising temperature, where ITO/WS$_2$/ENMO/CFTS/Au PSC indicated the highest value of ~27% and C$_{60}$ ETL-associated solar device showed the lowest value of ~23.8%. The FF of the WS$_2$ ETL-based solar configuration increased with the increase in temperature, where the largest value is ~81%. The FF of the C$_{60}$ ETL-associated solar device is also in an equivalent shape. On the other hand, the FF of PCBM ETL-associated solar configuration decreased with the increase in temperature. J_{SC} stays constant regardless of temperature changes in all three configurations. Which states that there is no impact of temperature on the J_{SC} of the PSCs of our study. All three structures showed a similar trend in V_{OC}, decreasing with higher temperatures. As the temperature increases, V_{OC} decreases due to bandgap narrowing and increased recombination.[91] While J_{SC} shows minor changes due to a balance between enhanced carrier generation and reduced mobility. The WS$_2$ ETL-based PSC indicated a maximum value of ~0.735 V, and the PCBM ETL-associated solar configuration displayed the smallest value of ~0.676 V. Moreover, rising

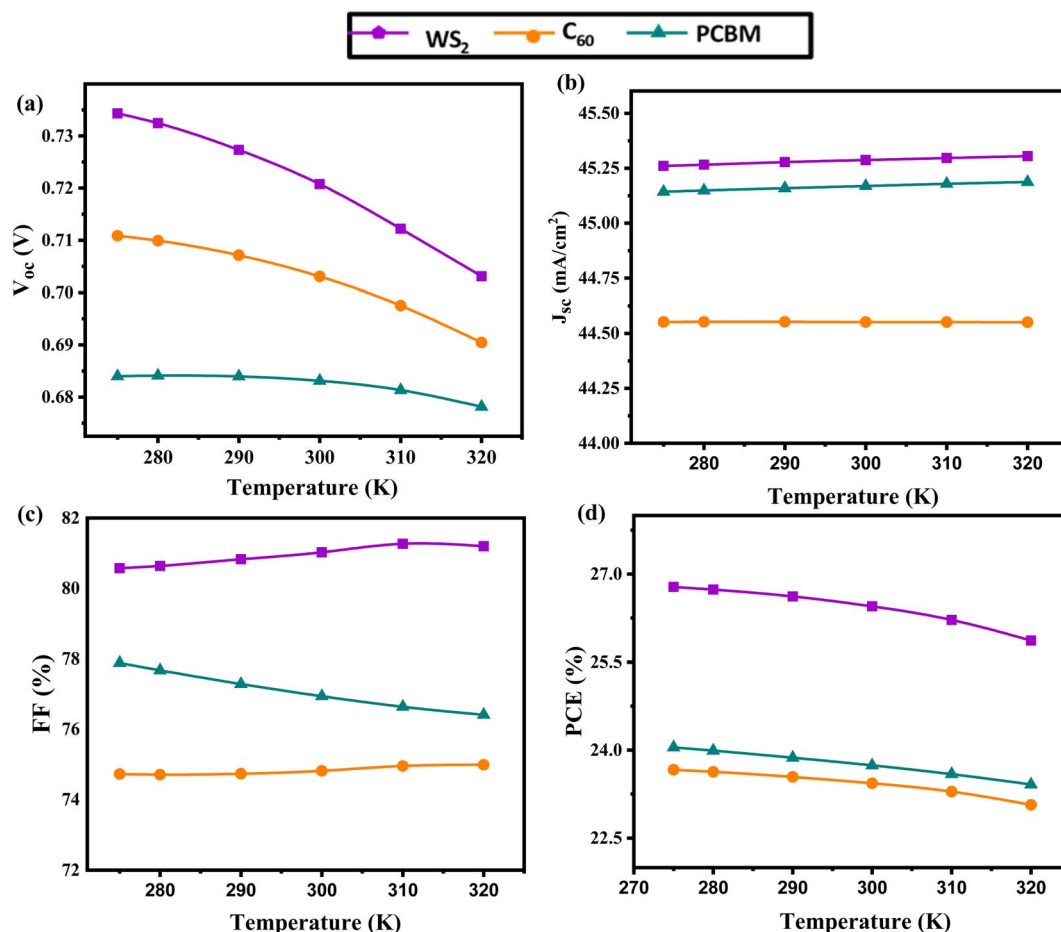Fig. 14 Effects of temperature on (a) V_{OC}, (b) J_{SC}, (c) FF, and (d) PCE for (ITO/ETL/Eu$_2$NiMnO$_6$/CFTS/Au) double PSCs using ETLs (WS$_2$, C$_{60}$, PCBM).

temperatures have an impact on diffusion length and raise R_S, which have an immediate impact on the device's FF and PCE.[92,93]

3.7. Influence of capacitance and Mott–Schottky

The capacitance per unit area (C) displayed with Mott–Schottky (MS) and bias voltage (V), respectively, for three distinct configurations are presented in Fig. 15(a) and (b). In both instances shown in Fig. 15, the frequency stayed at 1 MHz, while the voltage ranged from −0.8 V to 0.8 V. For all configurations, capacitance stays zero as voltage ranges between −0.8 V and 0.4 V, but when the voltage fluctuated between ∼0.4 to 0.8 V, all three PSCs showed an exponential increase, while the WS$_2$ ETL-associated solar configuration exhibited a late increase. The PSC with PCBM ETL demonstrated the peak capacitance of about 16 000 nF cm^{-2}, whereas the PSC with WS$_2$ ETL had the lowest capacitance at approximately 4000 nF cm^{-2}. Earlier research shows that the current is considerably less than the saturation current at low voltages and only reaches the saturation current at the peaks of voltage at the contact.[94]

Conversely, the built-in potential (V_{bi}) of a device reflects the difference in performance between the electrodes and the degree of doping, may be found using MS, a well-used and trustworthy technique.[80] Fig. 15(b) of our investigation showed

an almost exact reversal of the preceding Figure behavior, with each of the three PSCs exhibiting a linear drop while the voltage varied between −0.8 and 0.4 V and all three remaining constants when the voltage ranged between ∼0.4 and 0.8 V, when the value was zero. Here the C$_{60}$ ETL-associated structure indicated the largest MS value around 0.005 1/C^2 and the WS$_2$ ETL-associated structure revealed the smallest MS value around 0.0003 1/C^2.

3.8. Effects of generation rate and recombination rate

Fig. 15(c) and (d) provide the graphs illustrating the rates of generation and recombination for three distinct structures. As carriers are produced, an electron shifts to the conduction band, creating an electron–hole pair.[95] In Fig. 15(c), all three configurations show peak generation rates at about 0.8–0.9 μm. The computation of the electron–hole pair production, denoted as $G(x)$, is performed utilizing SCAPS-1D and the incoming photon flux, $N_{phot}(\lambda, x)$, according to eqn 11:

$$G(\lambda, x) = \alpha(\lambda, x) \times N_{phot}(\lambda, x) \tag{11}$$

The reverse of generation, known as recombination, is the coupling and annihilation of conduction band electrons and holes.[95] There is an impact on the defect state of every layer in
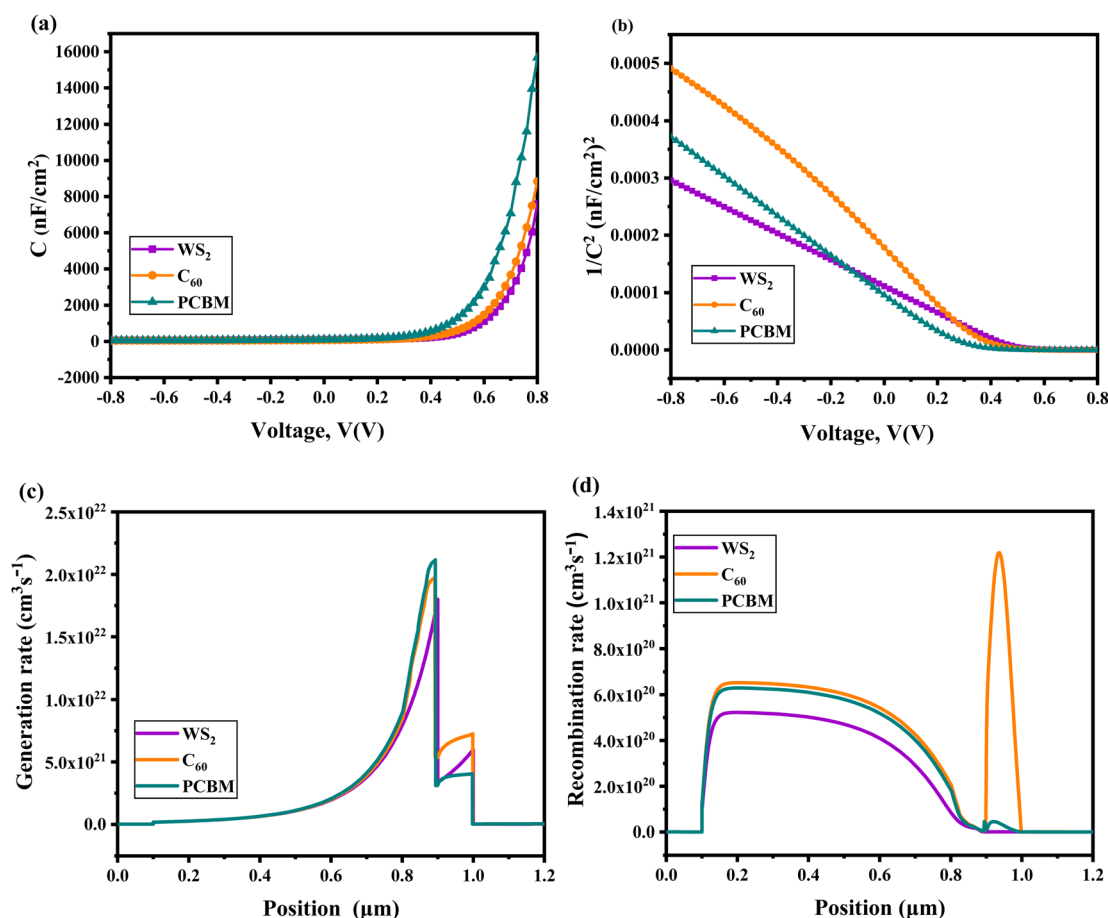

Fig. 15 Variation of (a) capacitance (b) Mott–Schottky (c) generation and (d) recombination for Eu$_2$NiMnO$_6$.

the recombination process. After that, the energy state is constructed, which has a great impact on the recombination process. Defects at interfaces and grain boundaries cause uneven recombination rates in PSCs.[86] Fig. 15(d) shows a slower start to recombination, with a peak at 0.9–1.0 μm in the C_{60} ETL structure. The convexity observed in the C_{60} and PCBM curves between 0.9–1.0 μm occurs due to the higher electron mobility of these materials, which results in increased charge buildup at the interface, leading to enhanced recombination.[96,97] In contrast, the WS_2 curve does not exhibit this convexity, as WS_2 demonstrates more uniform charge transport with reduced recombination effects, resulting in smoother behavior.[98] In the time range of 0.1–0.8 μm, the C_{60} and PCBM ETL-based structures showed almost similar recombination rates, at that time the WS_2 ETL-based PSC showed a slightly lower recombination rate. But, within the bounds of 1.0–1.2 μm, the recombination rates are almost zero for all three configurations.

3.9. *JV* and QE properties of Eu_2NiMnO_6

Fig. 16(a) shows the *J–V* curve for an ITO/ETL/ENMO/CFTS device structure with three distinct ETLs. In this case, the voltage varies between 0-0.8 V. In the beginning, all three configurations exhibit almost similar photocurrent. The process is continuous in the range of around 0.0–0.6 V for every structure, after that, the photocurrent of all PSCs start to decrease in the period of ∼0.6–0.72 V. Initially, the photocurrent of all three PSCs is nearly 45 mA cm^{-2}. Moreover, the WS_2 ETL-associated structure showed a good photocurrent in the presented Fig. 16(a), and the C_{60} ETL-based structure demonstrated a slightly reduced photocurrent as the voltage changed. The superior performance of WS_2 ETL-based devices in terms of photocurrent is due to better energy level alignment, higher charge mobility.[99] Conversely, the slightly reduced photocurrent with C_{60} is attributed to less optimal energy alignment, lower charge mobility, and possibly higher recombination rates.

The plots of QE for every device under study are displayed in Fig. 16(b). The wavelengths range from 300 to 1300 nm in this

case. In the plot, we observed an exponential increase for all configurations in the wavelength of 300–400 nm. It remains constant from ∼400–1000 nm, which is a long period. It can demonstrate that during that period, there is no impact of wavelength on the QE of studied PSCs. After that, the QE of all configurations starts to decrease with the variation of wavelength. In figure C_{60} the C_{60} ETL-based structure revealed a minor reduction in QE relative to other structures. However, the WS_2 and PCBM ETL-based configurations have displayed almost a similar kind of efficiency with the variation of wavelength. The reduced photon absorption in C_{60} might be the cause of the decreased QE.[88]

3.10. Effect of interface defect density

Interface defects play a crucial role in charge transport and overall device performance. At the ETL/ENMO interface, defect states can trap photogenerated electrons and enhance Shockley–Read–Hall (SRH) recombination, while at the ENMO/HTL interface, hole trapping similarly increases interfacial recombination, which negatively affects the V_{OC} and FF.[100] More defects at the interface lead to higher recombination and lower charge transport efficiency. Energy level alignment is also critical. A small positive conduction band offset (CBO) at the ETL/ENMO interface promotes efficient electron transfer, whereas a negative CBO encourages interface-assisted recombination.[101] Similarly, a slight positive valence band offset (VBO) at the ENMO/HTL interface enables hole extraction and suppresses electron leakage, while misalignment magnifies recombination losses.[102] In summary, minimizing interfacial defects, controlling defect density, and ensuring favorable energy alignment at both junctions are essential for efficient carrier transport and enhanced device performance.

Fig. 17(a) and (b) illustrate the influence of defect density (N_t) on the effects of the ETL/Eu_2NiMnO_6 and HTL/Eu_2NiMnO_6 interface on multiple photovoltaic parameters, including V_{OC}, FF, J_{SC}, and PCE, within the range of 10^{10} to 10^{18} cm^{-2}. According to the figure, recombination rates increase with

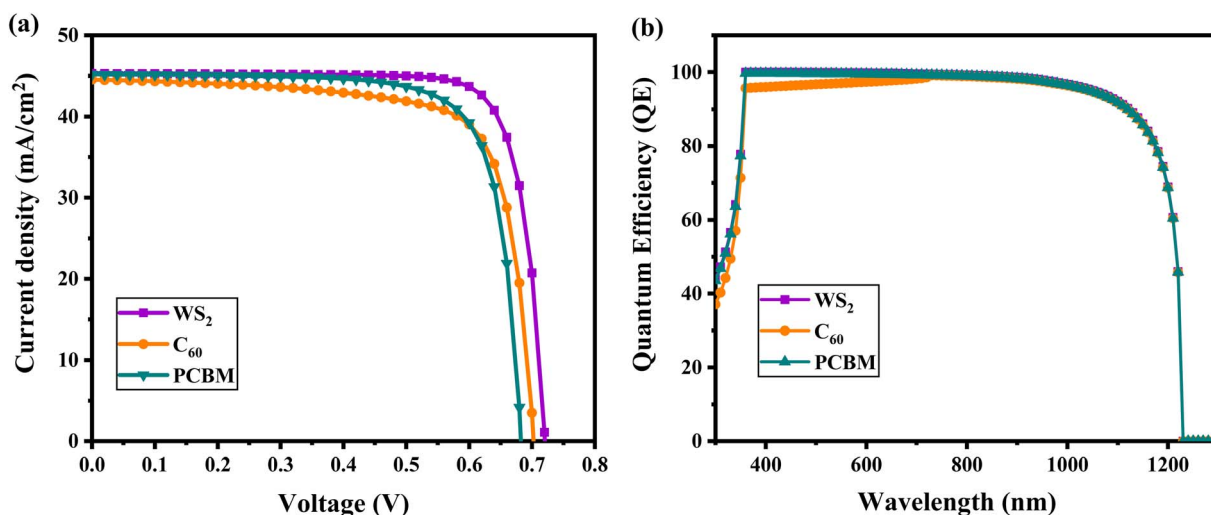**Fig. 16** (a) *J–V* curve and (b) QE curve optimization for Eu_2NiMnO_6.
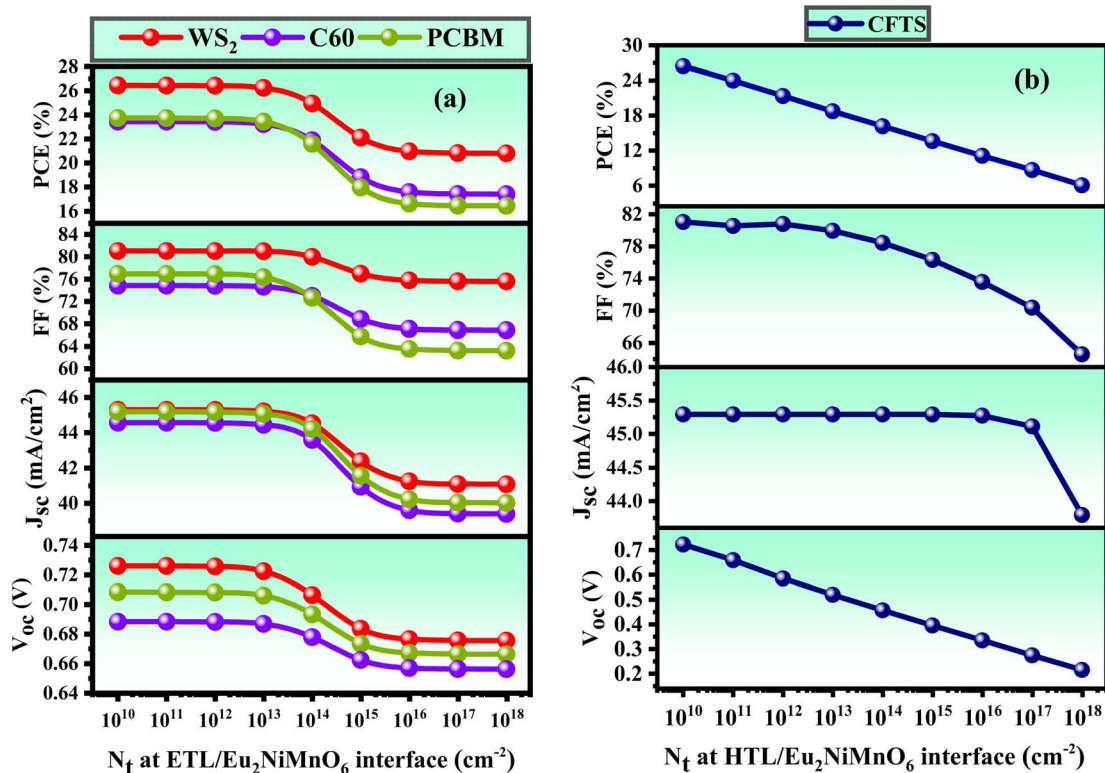
Fig. 17 Influence of interface defects between (a) ETL/Eu$_2$NiMnO$_6$ and (b) HTL/Eu$_2$NiMnO$_6$ on the V_{OC}, J_{SC}, FF, and PCE parameters.

rising N_t, reducing PCE, and ultimately leading to a fall in the performance parameters of PSCs. In this case, the performance parameters V_{OC}, FF, and PCE exhibit a declining trend as the defect density increases. The J_{SC} value remains almost constant for C$_{60}$ and PCBM-based structures. In terms of the WS$_2$-based ETL device, the J_{SC} value remained almost unchanged between defect density values of 10^{10} and 10^{16} cm^{-2}. Then, it displays a declining nature. The V_{OC} drops significantly from around 0.74 V to 0.22 V, the J_{SC} drops from nearly 45.3 to 43.81 mA cm^{-2}, and the FF decreases from around 81 to 64% for an ETL structure based on WS$_2$. As a result, the PCE reduces from approximately 27% to 5%, leading it the greatest among these three ETLs. To get the best performance, maintaining a defect density at 10^{10} cm^{-2} is crucial, which has been identified as the appropriate level for further investigation.

Eqn (12) defines the limit of interface recombination for the open-circuit voltage (V_{OC}).[103]

$$V_{OC} = \frac{1}{q}\left\{ \varnothing_c - AKT \ln\left(\frac{qN_V S_t}{J_{SC}}\right) \right\} \quad (12)$$

In the above formula, A defines the ideality factor, $\varnothing_c$ is the effective barrier height, and S_t specifies the recombination velocity at the interface.

Hole transport layers (HTLs) greatly influence photovoltaic (PV) device performance, with defect density serving as a crucial parameter. High defect concentrations (N_t) can restrict charge transfer, increase recombination events, and reduce the device's mechanical stability. In addition, inconsistent defects may alter the optical characteristics of the HTL, affecting

absorption and uniformity.[104] Ensuring low and uniform defect densities in HTLs is vital for achieving high efficiency and long-term durability. Fig. 17(b) presents the effect of interface defect density (N_t) on V_{OC}, FF, J_{SC}, and PCE for defect values between 10^{10}-10^{18} cm^{-2}. The Fig. 17 (b) shows that the HTL(CFTS)/Eu$_2$NiMnO$_6$ solar cell reaches its highest PCE of ~25.2% at $N_t = 10^{10}$ cm^{-2}, but efficiency decreases as defect density increases due to enhanced recombination losses. V_{OC} drops steadily from
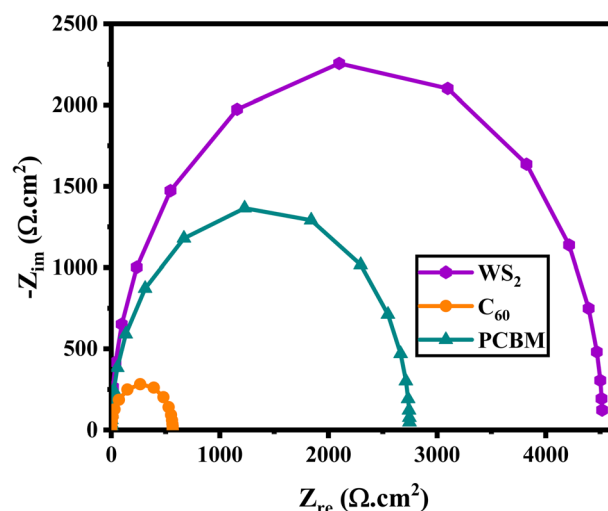

Fig. 18 Comparison of Nyquist plots for Eu$_2$NiMnO$_6$ absorbers with different ETL materials (WS$_2$, C$_{60}$, PCBM).

Table 4 Theoretical analysis of the ENMO absorber layer

Optimized devices	V_{OC} (V)	J_{SC} (mA cm^{-2})	FF (%)	PCE (%)	Ref.
FTO/TiO$_2$/ENMO/CuI/Au	0.772	16.43	74.16	9.41	62
FTO/TiO$_2$/ENMO/CuI/Au	0.78	21.5	75.33	12.63	108
ITO/WS$_2$/ENMO/CFTS/Au	0.720	45.2872	81.02	26.45	This study
ITO/C$_{60}$/ENMO/CFTS/Au	0.703	44.551	74.82	23.43	This study
ITO/PCBM/ENMO/CFTS/Au	0.683	45.16	76.94	23.74	This study

$\sim$0.74 V to $\sim$0.28 V with higher N_t, reflecting stronger non-radiative recombination. J_{SC} remains nearly constant ($\sim$45.6 mA cm^{-2}) up to 10^{16} cm^{-2} and then decreases at higher defect densities, while FF stays stable around 78% at low N_t but declines significantly beyond 10^{14} cm^{-2}.

3.11. Impedance effects on various optimized devices

The impedance, or Nyquist plot, of a solar cell allows for qualitative analysis of resistive losses, capacitance, and recombination issues.[105] The Nyquist plot shown in Fig. 18 provides a comprehensive understanding of the impedance characteristics of PSCs employing different ETL materials. The geometrical capacitance of the SC is depicted on the Y-axis, which indicates the buildup of carriers at the interface layers. Resistance arising from recombination is shown on the X-axis. It is apparent from the graph that the diameter of the semicircle varies for each ETL-based device. The WS$_2$ ETL-based structure's enlarged semicircle indicates a higher system impedance around 2200 ohm cm^2. The impedance of the WS$_2$ ETL-based structure is much greater than that of the other ETL-based designs. The C$_{60}$ ETL-based device had the smallest impedance, observing around 270 ohm cm^2. High-frequency measurements of resistance indicate the material's recombination resistance. The capacitance at these frequencies reflects the value of geometric capacitance, indicating that charge accumulates at the interfaces.[106] Considering hysteresis and ionic mobility, the low-frequency response is more suspicious.[107] A complete analysis of the impedance properties for PSCs is provided by the Nyquist plot. It elucidates the influence of various materials on ETL in terms of capacitance, resistive losses, and recombination rates. This comprehension is critical to the optimal and steady operation of solar cell devices.

3.12. SCAPS-1D results compared to previous work

Table 4 compares photovoltaic parameters of previous solar cells with the same absorber to optimized ENMO-based PSCs. The previously published structure is FTO/TiO$_2$/ENMO/CuI/Au, with the efficiency of these theoretical results, is 9.41%[62] and 12.63%.[108] The calculated PCE for the solar structures presented for ITO/WS$_2$/ENMO/CFTS/Au, ITO/C$_{60}$/ENMO/CFTS/Au and ITO/PCBM/ENMO/CFTS/Au is 26.45, 23.43, and 23.74%, which exceeds the theoretical results reported in earlier studies. The main reason for the difference is the careful selection of ETL and HTL contributed to higher J_{SC} values in our devices. We investigated absorber characteristics, such as thickness, which vary from those in previous theoretical studies of device structures. Furthermore, the combinations of ETL and HTL we explored differ from those studied in earlier theoretical research. Additionally, the optical properties vary between different absorbers, leading to differences in solar energy absorption. The ENMO-based PSC design exhibits FF values comparable to those found in earlier research.

4 Conclusion

The primary purpose of this research is to explore the double perovskite Eu$_2$NiMnO$_6$'s (ENMO) ability to develop useful photovoltaic applications utilizing the SCAPS-1D tool findings. It is discovered that the three solar configurations-ITO/WS$_2$/ENMO/CFTS/Au, ITO/C$_{60}$/ENMO/CFTS/Au, and ITO/PCBM/ENMO/CFTS/Au-are the best SC configurations in terms of PV characteristics. The WS$_2$-based structure exhibited the highest performance with a V_{OC} of 0.7208 V, a J_{SC} of 45.78 mA cm^{-2}, an FF of 81.02%, and a PCE of 26.45%. This study examined the effects of various PV parameters while varying absorber thickness (0.4 to 1.4 μm). From 0.4–0.8, μm the curve is inclined, and the best efficiency we got for the absorber thickness is 0.8 μm, for all the configurations, and after the rate of efficiency is almost constant. Then HTL is observed at (0.1 to 0.5 μm), where we notice that for all device configurations with a variation of HTL thickness, efficiency is nearly constant. The impact of variations in acceptor density (N_A) was also investigated in this study. Acceptor density from 7×10^{14} cm^{-3} to 7×10^{18} cm^{-3} revealed insights into the performance variations. Since shunt resistance enhances V_{OC}, FF, PCE, and J_{SC} have a steady, negligible influence, and series resistance decreases PCE, FF, J_{SC}, and V_{OC} almost constantly. There is a considerable effect of temperature for all three configurations. The devices linked with PCBM and C$_{60}$ ETLs exhibited the maximum rates of generation and recombination at (0.8–0.9) μm and (0.9–1) μm, respectively. Compared to other ETL-associated devices, the WS$_2$ ETL device's appropriate band alignment resulted in superior J–V and QE characteristics. These results have great significance for researchers exploring double perovskite-based PSCs since they allow for the creation of ideal SC configurations before the manufacturing and testing of these devices.

Author contributions

Md. Abu Bakkar Siddique: Investigation, methodology, data curation, conceptualization, writing original manuscript; Nazmul Shahadath: Investigation, methodology, data curation, review-editing; Md. Tarekuzzaman: Formal analysis, software,

conceptualization, review-editing; Md. Raihan Kabir: Formal analysis, methodology, data curation, review-editing; Sohail Ahmad: Data curation, validation, Formal analysis; Rashel Mohammad Khokan: Formal analysis, validation, supervision, review-editing. Md. Rasheduzzaman: Formal analysis, validation, review-editing; S. M. G Mostafa: Formal analysis, validation, review-editing; Mohammad Jalal Uddin Formal analysis, validation, review-editing; Md. Zahid Hasan: Formal analysis, validation, supervision, review-editing.

Conflicts of interest

There is no conflict to declare.

Abbreviations

PSC	Perovskite solar cell
PCE	Power conversion efficiency
J_{SC}	Short-circuit current density
V_{OC}	Open-circuit voltage
FF	Fill factor
ITO	Indium tin oxide
PV	Photovoltaic
J–V	Current density–voltage
WS_2	Tungsten disulfide
C_{60}	Buckminsterfullerene
E_A	Electron affinity
ε_r	Dielectric permittivity (relative)
N_C	CB effective density of states
N_D	Shallow uniform donor density
N_t	Defect density
PCBM	Phenyl-C_{61}-butyric acid methyl ester
CBTS	Copper barium tin sulfide
MS	Mott–Schottky
QE	Quantum efficiency
WF	Work function
$F_{n/p}$	Fermi level of the electron/hole
Au	Gold
E_C/E_V	Energy level of the conduction/valence band
Al	Aluminium
SC	Solar cell
N_V	VB effective density of states
μ_n	Electron mobility
μ_h	Hole mobility
N_A	Shallow uniform acceptor density
CFTS	Copper ferrite tin sulfide

Data availability

Data will be made available on request. The SCAPS-1D program was graciously provided by Dr M. Burgelman of the University of Gent in Belgium, for which the authors extend their sincere gratitude.

Supplementary information is available. See DOI: **https://doi.org/10.1039/d5ra05366h**.

References

1 M. Asif and T. Muneer, *Renew. Sustain. Energy Rev.*, 2007, **11**, 1388–1413.

2 M. H. K. Rubel, S. K. Mitro, M. K. Hossain, K. M. Hossain, M. M. Rahaman, J. Hossain, B. K. Mondal, A. Akter, Md. F. Rahman, I. Ahmed and A. K. M. A. Islam, *Mater. Today Commun.*, 2022, **33**, 104302.

3 S. Saurabh, M. K. Hossain, S. Singh, S. K. Agnihotri and D. P. Samajdar, *RSC Adv.*, 2023, **13**, 9878–9891.

4 H. Al-Dmour, R. H. Alzard, H. Alblooshi, K. Alhosani, S. AlMadhoob and N. Saleh, *Front. Chem.*, 2019, **7**, 561.

5 H. Al-Dmour and D. M. Taylor, *Thin Solid Films*, 2011, **519**, 8135–8138.

6 N. Shahadath, Md. A. B. Siddique, Md. Tarekuzzaman, M. H. Ishraq, Md. F. Rahman, A. M. Arfi, Md. Rasheduzzaman, S. M. G. Mostafa and Md. Z. Hasan, *New J. Chem.*, 2024, **48**, 14336–14353.

7 E. Kabir, P. Kumar, S. Kumar, A. A. Adelodun and K.-H. Kim, *Renew. Sustain. Energy Rev.*, 2018, **82**, 894–900.

8 E. Oublal, M. Al-Hattab, A. Ait Abdelkadir and M. Sahal, *Sol. Energy*, 2022, **246**, 57–65.

9 H.-H. Huang, Y.-C. Shih, L. Wang and K.-F. Lin, *Energy Environ. Sci.*, 2019, **12**, 1265–1273.

10 Md. A. Bakkar Siddique, Md. S. Parves, Md. Tarekuzzaman, Md. R. Kabir, M. S. M. Al-Saleem, J. Y. Al-Humaidi, Md. Rasheduzzaman, M. M. Hossen, M. M. Rahman and Md. Z. Hasan, *Langmuir*, 2025, **41**, 19797–19820.

11 X. Wang, T. Zhang, Y. Lou and Y. Zhao, *Mater. Chem. Front.*, 2019, **3**, 365–375.

12 A. Miyata, A. Mitioglu, P. Plochocka, O. Portugall, J. T. Wang, S. D. Stranks, H. J. Snaith and R. J. Nicholas, *Nat. Phys.*, 2015, **11**(7), 582–587.

13 J. Huang, Y. Yuan, Y. Shao and Y. Yan, *Nat. Rev. Mater.*, 2017, **2**(7), 1–9.

14 M. A. Madanat, A. A. Al-Tabbakh, M. Alsa'eed, H. Al-Dmour and M. S. Mousa, *Ultramicroscopy*, 2022, **234**, 113479.

15 J. J. Yoo, G. Seo, M. R. Chua, T. G. Park, Y. Lu, F. Rotermund, Y. K. Kim, C. S. Moon, N. J. Jeon, J. P. Correa-Baena and V. Bulović, *Nature*, 2021, **590**(7847), 587–593.

16 J. Jeong, M. Kim, J. Seo, H. Lu, P. Ahlawat, A. Mishra, Y. Yang, M. A. Hope, F. T. Eickemeyer, M. Kim, Y. J. Yoon, I. W. Choi, B. P. Darwich, S. J. Choi, Y. Jo, J. H. Lee, B. Walker, S. M. Zakeeruddin, L. Emsley, U. Rothlisberger, A. Hagfeldt, D. S. Kim, M. Grätzel and J. Y. Kim, *Nature*, 2021, **592**, 381–385.

17 T. J. Macdonald, M. Batmunkh, C.-T. Lin, J. Kim, D. D. Tune, F. Ambroz, X. Li, S. Xu, C. Sol, I. Papakonstantinou, M. A. McLachlan, I. P. Parkin, J. G. Shapter and J. R. Durrant, *Small Methods*, 2019, **3**, 1900164.

18 M. Saliba, J.-P. Correa-Baena, C. M. Wolff, M. Stolterfoht, N. Phung, S. Albrecht, D. Neher and A. Abate, *Chem. Mater.*, 2018, **30**, 4193–4201.

19 A. M. Alanazi, H. Al Dmour, S. A. Popoola, H. Oudghiri Hassani, S. Rakass, R. Al-Faze and F. Kooli, *Inorganics*, 2023, **11**, 423.

20 M. R. Kabir, M. H. Ishraq, M. Tarekuzzaman, N. I. Nahid, J. K. Modak, S. Ahmad, A. M. Arfi, M. Rasheduzzaman and M. Z. Hasan, *Eng. Res. Express*, 2025, **7**, 015319.

21 T. I. Alanazi, O. S. Game, J. A. Smith, R. C. Kilbride, C. Greenland, R. Jayaprakash, K. Georgiou, N. J. Terrill and D. G. Lidzey, *RSC Adv.*, 2020, **10**, 40341–40350.

22 S. Abdelaziz, A. Zekry, A. Shaker and M. Abouelatta, *Opt. Mater.*, 2022, **123**, 111893.

23 Z. T. M. Noori, A. M. Naji, O. A. Nief, M. K. A. Mohammed, N. M. Ahmed and S. Singh, *Int. J. Energy Res.*, 2022, **46**, 17285–17294.

24 S. Al-Taweel, S. Al-Trawneh, H. Al-Dmour, O. Al-Gzawat, W. Alhalasah and M. Mousa, *Heliyon*, 2023, **9**, e21039.

25 Md. R. Kabir, N. Shahadath, Md. Tarekuzzaman, Md. A. B. Siddique, O. Alsalmi, Md. Rasheduzzaman, M. A. Qader, M. M. Hossen and Md. Z. Hasan, *RSC Adv.*, 2025, **15**, 17906–17932.

26 T. He, Y. Jiang, X. Xing and M. Yuan, *Adv. Mater.*, 2020, **32**(26), 1903937.

27 A. N. Singh, S. Kajal, J. Kim, A. Jana, J. Y. Kim and K. S. Kim, *Adv. Energy Mater.*, 2020, **10**, 2070129.

28 J. Xu, R. Saklatvala, S. Mittal, S. Deshmukh and A. Procopio, *Adv. Sci.*, 2020, **7**, 1903394.

29 S. Kashyap, J. Madan, M. K. A. Mohammed, M. Khalid Hossain, S. Ponnusamy and R. Pandey, *Mater. Lett.*, 2023, **339**, 134096.

30 M. K. A. Mohammed, A. K. Al-Mousoi, S. Singh, A. Kumar, M. K. Hossain, S. Q. Salih, P. Sasikumar, R. Pandey, A. A. Yadav and Z. M. Yaseen, *Opt. Mater.*, 2023, **138**, 113702.

31 R. Pandey, S. Bhattarai, K. Sharma, J. Madan, A. K. Al-Mousoi, M. K. Mohammed and M. K. Hossain, *ACS Appl. Electron. Mater.*, 2023, **5**(10), 5303–5315.

32 M. K. Hossain, A. A. Arnab, D. P. Samajdar, M. H. K. Rubel, M. M. Hossain, Md. R. Islam, R. C. Das, H. Bencherif, Md. F. Rahman, J. Madan, R. Pandey, S. Bhattarai, M. Amami and D. K. Dwivedi, *Energy Fuels*, 2023, **37**, 13377–13396.

33 H. J. Snaith, *J. Phys. Chem. Lett.*, 2013, **4**, 3623–3630.

34 M. Faizan, G. Murtaza, S. H. Khan, A. Khan, A. Mehmood, R. Khenata and S. Hussain, *Bull. Mater. Sci.*, 2016, **39**, 1419–1425.

35 A. Schmitz, L. L. Schaberg, S. Sirotinskaya, M. Pantaler, D. C. Lupascu, N. Benson and G. Bacher, *ACS Energy Lett.*, 2020, **5**, 559–565.

36 Md. Sariful Sheikh, D. Ghosh, A. Dutta, S. Bhattacharyya and T. P. Sinha, *Mater. Sci. Eng. B*, 2017, **226**, 10–17.

37 M. K. Hossain, G. F. I. Toki, A. Kuddus, M. H. K. Rubel, M. M. Hossain, H. Bencherif, Md. F. Rahman, Md. R. Islam and M. Mushtaq, *Sci. Rep.*, 2023, **13**, 2521.

38 Y. Raoui, H. Ez-Zahraouy, N. Tahiri, O. El Bounagui, S. Ahmad and S. Kazim, *Sol. Energy*, 2019, **193**, 948–955.

39 N. Singh, A. Agarwal and M. Agarwal, *Opt. Mater.*, 2021, **114**, 110964.

40 K. Sekar, L. Marasamy, S. Mayarambakam, H. Hawashin, M. Nour and J. Bouclé, *RSC Adv.*, 2023, **13**, 25483–25496.

41 M. Elhamel, Z. Hebboul, M. E. Naidjate, A. Draoui, A. Benghia, M. abdelilah Fadla, M. B. Kanoun and S. Goumri-Said, *J. Solid State Chem.*, 2023, **323**, 124022.

42 H. M. Christen and G. Eres, *J. Phys. Condens. Matter*, 2008, **20**, 264005.

43 S. M. AL-Shomar, *Mater. Res. Express*, 2021, **8**, 026402.

44 A. K. Al-Mousoi, M. K. Mohammed, A. Kumar, R. Pandey, J. Madan, D. Dastan, M. K. Hossain, P. Sakthivel and Z. M. Yaseen, *Phys. Chem. Chem. Phys.*, 2023, **25**(24), 16459–16468.

45 M. F. Rahman, N. Mahmud, I. Alam, M. H. Ali, M. M. Moon, A. Kuddus, G. F. Toki, M. H. Rubel, M. A. Al Asad and M. K. Hossain, *AIP Adv.*, 2023, **13**(4), 045309.

46 Md. Hasan Ali, A. T. M. Saiful Islam, M. D. Haque, Md. Ferdous Rahman, M. Khalid Hossain, N. Sultana and A. Z. M. Touhidul Islam, *Mater. Today Commun.*, 2023, **34**, 105387.

47 A. Isha, A. Kowsar, A. Kuddus, M. K. Hossain, M. H. Ali, M. D. Haque and M. F. Rahman, *Heliyon*, 2023, **9**, e15716.

48 M. H. Ali, M. A. Al Mamun, M. D. Haque, M. F. Rahman, M. K. Hossain and A. Z. Md Touhidul Islam, *ACS Omega*, 2023, **8**(7), 7017–7029.

49 Md. F. Rahman, Md. M. Alam Moon, M. K. Hossain, Md. H. Ali, Md. D. Haque, A. Kuddus, J. Hossain and A. B. Md. Ismail, *Heliyon*, 2022, **8**, e12034.

50 D. Dastan, M. K. Mohammed, A. K. Al-Mousoi, A. Kumar, S. Q. Salih, P. S. JosephNg, D. S. Ahmed, R. Pandey, Z. M. Yaseen and M. K. Hossain, *Sci. Rep.*, 2023, **13**(1), 9076.

51 M. Minbashi, A. Ghobadi, M. H. Ehsani, H. Rezagholipour Dizaji and N. Memarian, *Sol. Energy*, 2018, **176**, 520–525.

52 S. M. Sze, Y. Li and K. K. Ng, *Physics of Semiconductor Devices*, John wiley & sons, 2021.

53 M. K. Hossain, M. H. Rubel, G. I. Toki, I. Alam, M. F. Rahman and H. Bencherif, *ACS Omega*, 2022, **7**(47), 43210–43230.

54 S. Bhattarai and T. D. Das, *Sol. Energy*, 2021, **217**, 200–207.

55 M. S. Sheikh, A. P. Sakhya, A. Dutta and T. P. Sinha, *Comput. Mater. Sci.*, 2019, **161**, 293–299.

56 D. C. Kakarla, K. M. Jyothinagaram, A. K. Das and V. Adyam, *J. Am. Ceram. Soc.*, 2014, **97**, 2858–2866.

57 M. Nasir, S. Kumar, N. Patra, D. Bhattacharya, S. N. Jha, D. R. Basaula, S. Bhatt, M. Khan, S. W. Liu, S. Biring and S. Sen, *arXiv*, 2018, DOI: **10.48550/ARXIV.1808.00170**.

58 C. Chen, X. Lu, X. Hu, G. Liang and G. Fang, *J. Mater. Chem. C*, 2024, **12**, 16–28.

59 H. Dixit, N. K. Bansal, S. Porwal, D. Kumar and T. Singh, *Optik*, 2023, **295**, 171474.

60 A. Talukdar, P. Debnath, J. Sarkar and S. Chatterjee, *Indian J. Phys.*, 2024, **98**, 3913–3929.

61 M. A. Nalianya, C. Awino, H. Barasa, V. Odari, F. Gaitho, B. Omogo and M. Mageto, *Optik*, 2021, **248**, 168060.

62 M. Kumar, A. Raj, A. Kumar and A. Anshul, *Mater. Today Commun.*, 2021, **26**, 101851.

63 M. H. Ishraq, Md. R. Kabir, Md. Tarekuzzaman, Md. F. Rahman, Md. Rasheduzzaman and Md. Z. Hasan, *Adv. Theory Simul.*, 2024, 2400360.

64 C. Walkons, R. Murshed and S. Bansal, *Sol. RRL*, 2020, **4**(10), 2000299.

65 T. Minemoto and M. Murata, *Sol. Energy Mater. Sol. Cells*, 2015, **133**, 8–14.

66 W. Tress, *Adv. Energy Mater.*, 2017, **7**, 1602358.

67 Y.-N. Zhang, B. Li, L. Fu, Y. Zou, Q. Li and L.-W. Yin, *Sol. Energy Mater. Sol. Cells*, 2019, **194**, 168–176.

68 F. Xu, X. Yang, T. Huang, Z. Li, Y. Ji and R. Zhu, *Nano Energy*, 2024, **130**, 110171.

69 M. A. Green, A. Ho-Baillie and H. J. Snaith, *Nat. Photonics*, 2014, **8**, 506–514.

70 Y. Zhao and K. Zhu, *J. Phys. Chem. Lett.*, 2013, **4**, 2880–2884.

71 J.-F. Liao, W.-Q. Wu, Y. Jiang, J.-X. Zhong, L. Wang and D.-B. Kuang, *Chem. Soc. Rev.*, 2020, **49**, 354–381.

72 H. Wang, H. Li, W. Cai, P. Zhang, S. Cao, Z. Chen and Z. Zang, *Nanoscale*, 2020, **12**, 14369–14404.

73 M. Khalid Hossain, G. F. Ishraque Toki, I. Alam, R. Pandey, D. P. Samajdar, M. Ferdous Rahman, M. Rasidul Islam, M. H. K. Rubel, H. Bencherif, J. Madan and M. K. A. Mohammed, *New J. Chem.*, 2023, **47**, 4801–4817.

74 Z. Iqbal, F. Zu, A. Musiienko, E. Gutierrez-Partida, H. Köbler, T. W. Gries, G. V. Sannino, L. Canil, N. Koch, M. Stolterfoht, D. Neher, M. Pavone, A. B. Muñoz-García, A. Abate and Q. Wang, *ACS Energy Lett.*, 2023, **8**, 4304–4314.

75 J. Siekmann, A. Kulkarni, S. Akel, B. Klingebiel, M. Saliba, U. Rau and T. Kirchartz, *Adv. Energy Mater.*, 2023, **13**, 2300448.

76 E. I. Emon, A. M. Islam, M. K. Sobayel, S. Islam, M. Akhtaruzzaman, N. Amin, A. Ahmed and M. J. Rashid, *Heliyon*, 2023, **9**, e14438.

77 M. A. Green, *Solid-State Electron.*, 1981, **24**, 788–789.

78 M. T. Dang, L. Hirsch and G. Wantz, *Adv. Mater.*, 2011, **23**, 3597–3602.

79 R. R. Scherberger, H. Kaess and S. Brückner, *Arzneimittelforschung*, 1975, **25**, 1460–1463.

80 I. Alam, R. Mollick and M. A. Ashraf, *Phys. B*, 2021, **618**, 413187.

81 A. S, N. Abraham and V. Suresh Babu, *Mater. Today: Proc.*, 2021, **43**, 3432–3437.

82 J. Xu, O. Voznyy, R. Comin, X. Gong, G. Walters, M. Liu, P. Kanjanaboos, X. Lan and E. H. Sargent, *Adv. Mater.*, 2016, **28**, 2807–2815.

83 O. Saidani, S. Goumri-Said, A. Yousfi, G. S. Sahoo and M. B. Kanoun, *RSC Adv.*, 2025, **15**, 7342–7353.

84 N. Marinova, W. Tress, R. Humphry-Baker, M. I. Dar, V. Bojinov, S. M. Zakeeruddin, M. K. Nazeeruddin and M. Grätzel, *ACS Nano*, 2015, **9**, 4200–4209.

85 A. Owolabi, M. Onimisi, J. Ukwenya, A. Bature, U. Ushiekpan and U. Ushiekpan, *Am. J. Phys. Appl.*, 2020, **8**, 8–18.

86 M. K. Hossain, D. P. Samajdar, R. C. Das, A. A. Arnab, Md. F. Rahman, M. H. K. Rubel, Md. R. Islam, H. Bencherif, R. Pandey, J. Madan and M. K. A. Mohammed, *Energy Fuels*, 2023, **37**, 3957–3979.

87 L. Lin, L. Jiang, P. Li, B. Fan and Y. Qiu, *J. Phys. Chem. Solids*, 2019, **124**, 205–211.

88 M. K. Hossain, G. F. Ishraque Toki, D. P. Samajdar, M. H. K. Rubel, M. Mushtaq, Md. R. Islam, Md. F. Rahman, S. Bhattarai, H. Bencherif, M. K. A. Mohammed, R. Pandey and J. Madan, *Energy Fuels*, 2023, **37**, 7380–7400.

89 M. N. H. Riyad, A. Sunny, M. M. Khatun, S. Rahman and S. R. A. Ahmed, *Eng. Rep.*, 2023, **5**, e12600.

90 A. Sunny, S. Rahman, M. M. Khatun and S. R. A. Ahmed, *AIP Adv.*, 2021, **11**, 065102.

91 A. K. Thakur, G. Wantz, G. Garcia-Belmonte, J. Bisquert and L. Hirsch, *Sol. Energy Mater. Sol. Cells*, 2011, **95**, 2131–2135.

92 F. Behrouznejad, S. Shahbazi, N. Taghavinia, H. P. Wu and E. W. Diau, *J. Mater. Chem. A*, 2016, **4**(35), 13488–13498.

93 S. R. Raga, E. M. Barea and F. Fabregat-Santiago, *J. Phys. Chem. Lett.*, 2012, **3**, 1629–1634.

94 M. Burgelman, K. Decock, A. Niemegeers, J. Verschraegen and S. Degrave, *SCAPS manual*, University of Ghent, Ghent, Belgium, 2016.

95 M. K. Hossain, A. A. Arnab, R. C. Das, K. M. Hossain, M. H. Rubel, M. F. Rahman, H. Bencherif, M. E. Emetere, M. K. Mohammed and R. Pandey, *RSC Adv.*, 2022, **12**(54), 35002–35025.

96 V. M. Caselli and T. J. Savenije, *J. Phys. Chem. Lett.*, 2022, **13**, 7523–7531.

97 N. K. Elumalai, L. M. Yin, V. Chellappan, Z. Jie, Z. Peining and S. Ramakrishna, *Phys. Status Solidi A*, 2012, **209**, 1592–1597.

98 L. Wang, M. Tahir, H. Chen and J. B. Sambur, *Nano Lett.*, 2019, **19**, 9084–9094.

99 M. Malik, M. Kashif, F. B. Sumona and M. U. N. Tariq, *J. Opt.*, 2025, **27**, 015901.

100 F. Izadi, A. Ghobadi, A. Gharaati, M. Minbashi and A. Hajjiah, *Optik*, 2021, **227**, 166061.

101 Z. Zhao, Y. Liu, D. Wang, C. Ling, Q. Chang, J. Li, Y. Zhao and H. Jin, *Sol. Energy Mater. Sol. Cells*, 2020, **209**, 110443.

102 C. Ding, Y. Zhang, F. Liu, Y. Kitabatake, S. Hayase, T. Toyoda, K. Yoshino, T. Minemoto, K. Katayama and Q. Shen, *Nano Energy*, 2018, **53**, 17–26.

103 G. G. Malliaras, J. R. Salem, P. J. Brock and C. Scott, *Phys. Rev. B:Condens. Matter Mater. Phys.*, 1998, **58**, R13411–R13414.

104 M. Reza, A. Ghosh, M. Reza, S. N. Wornob and S. Sultana, *Energy Nexus*, 2025, **18**, 100417.

105 S. Bhattarai, R. Pandey, J. Madan, S. Tayeng, P. K. Kalita, M. Z. Ansari, L. B. Farhat, M. Amami and M. K. Hossain, *RSC Adv.*, 2023, **13**(38), 26851–26860.

106 E. von Hauff and D. Klotz, *J. Mater. Chem. C*, 2022, **10**, 742–761.

107 A. Guerrero, J. Bisquert and G. Garcia-Belmonte, *Chem. Rev.*, 2021, **121**, 14430–14484.

108 A. Raj, A. Anshul and M. Kumar, *Mater. Today: Proc.*, 2022, **67**, 748–751.